Space Weather

RESEARCH ARTICLE
10.1029/2023SW003443

An Efficient, Time-Dependent High Speed Stream Model and Application to Solar Wind Forecasts

C. Kay[1,2], T. Nieves-Chinchilla[1], S. J. Hofmeister[3], and E. Palmerio[4]

[1]Heliophysics Science Division, NASA Goddard Space Flight Center, Greenbelt, MD, USA, [2]Department of Physics, The Catholic University of America, Washington, DC, USA, [3]Leibniz Institute for Astrophysics, Potsdam, Germany, [4]Predictive Science Inc., San Diego, CA, USA

Key Points:

- Mostly Empirical Operation Wind with a High Speed Stream (MEOW-HiSS) is a new, time-dependent, empirical model that simulates radial profiles of high speed streams (HSS) below 1.5 au
- MEOW-HiSS accurately reproduces the density, velocity, magnetic field, and temperature of the original magnetohydrodynamic simulation upon which it is based
- We present a method to determine MEOW-HiSS inputs from observations and show that it can reproduce in situ HSS seen at 1 au

Supporting Information:

Supporting Information may be found in the online version of this article.

Correspondence to:

C. Kay,
christina.d.kay@nasa.gov

Citation:

Kay, C., Nieves-Chinchilla, T., Hofmeister, S. J., & Palmerio, E. (2023). An efficient, time-dependent high speed stream model and application to solar wind forecasts. *Space Weather*, *21*, e2023SW003443. https://doi.org/10.1029/2023SW003443

Received 26 JAN 2023
Accepted 26 APR 2023

Abstract Predicting space weather effects of the solar wind requires knowing the location and properties of any embedded high speed streams (HSSs) or stream interactions regions (SIRs) that form as the fast solar wind catches up to slow preceding wind. Additionally, this background solar wind affects the evolution of coronal mass ejections. We present the Mostly Empirical Operation Wind with a High Speed Stream (MEOW-HiSS) model, which runs nearly instantaneously. This model is derived from magnetohydrodynamic (MHD) simulations of an idealized HSS emanating from a circular coronal hole. We split the MHD HSS radial profiles into small regions well-described by simple functions (e.g., flat, linear, exponential, sinusoidal) that can be constrained using the MHD values. We then determine how the region boundaries and the constraining values change with CH area and the radial distance of the HSS front. MEOW-HiSS only requires this area and distance to reproduce the corresponding radial profile with an error of less than 10% for most parameters. MEOW-HiSS produces profiles at any subsequent times with almost no loss in accuracy. We compare MEOW-HiSS results to four HSS observed in situ at 1 au. We present a method for determining MEOW-HiSS inputs from extreme ultra-violet images and use these values to hindcast the observed cases. We find average accuracies of 2.8 cm^{-3} in the number density (50% error over the full profile), 56.7 km/s in the radial velocity (10%), 2.2 nT in the absolute radial magnetic field (50%), 1.6 nT in the absolute longitudinal magnetic field (50%), and 7×10^4 K in the temperature (50%).

Plain Language Summary A flow of plasma continuously leaves the Sun, forming a solar wind. The solar wind have fast and slow components, which have different sources on the solar surface. As the Sun rotates, different sources appear along a path. If fast wind leaves the Sun behind slow wind, the fast wind can catch up to the slow wind and begin interacting. The slow wind will build up in front of the fast wind in a stream interaction region (SIR) with enhanced density and magnetic field strength. Knowing where high speed streams (HSSs) and the associated SIRs are is important to predict any space weather effects. HSSs and SIRs have been previously modeled with sophisticated but computationally expensive simulations. Here, we tune a very simple, empirical model to reproduce the results of the sophisticated models. We show that this new, nearly instantaneous model essentially matches the previous results and that it can reproduce observed events near the Earth.

1. Introduction

A continuous stream of plasma blows out from the solar atmosphere, spreading out into interplanetary space. This so-called *solar wind* is not uniform, but rather contains distinct regions of fast (≳600 km/s) and slow (300–400 km/s) plasma flows. The fast solar wind is known to originate along the open magnetic field lines emanating from coronal holes (CHs; e.g., Cranmer, 2009) but there is less consensus on the source of the slow wind (see Cranmer et al., 2017, for a review on the origins of the ambient solar wind). Possible sources of the slow wind that have been proposed in the literature include helmet streamers (e.g., Einaudi et al., 1999), pseudo-streamers (e.g., Riley & Luhmann, 2012), coronal loops (e.g., Fisk, 2003), active regions (e.g., Harra et al., 2008), CH boundaries (e.g., Schwadron et al., 2005), and even small equatorial CHs (e.g., Bale et al., 2019).

Beyond the corona, interesting structures can develop as the fast and slow solar wind interact. As the Sun rotates, different sources of solar wind rotate onto a given radial trajectory, transforming variations in longitude to variations in time, which become variations in radial distance. As a CH rotates around, we expect the solar wind to increase from slow ambient values near the leading boundary, into a plateau of fast wind within the core of the

CH, followed by a tail decreasing back to the ambient values toward the trailing edge of the CH. In interplanetary space, this structure is typically known as a high speed stream (HSS).

As the HSS has a higher speed than the ambient solar wind, as it moves out in interplanetary space it begins compressing the upstream slow solar wind, forming a stream interaction region (SIR; e.g., Richardson, 2018), which separates the fast wind from the unperturbed upstream slow solar wind. Within this article, we will refer to the full structure (SIR, plateau, and tail) as a HSS. Significant compression occurs within the SIR as slow wind piles up in front of the fast wind, which enhances the number density and magnetic field strength in this region. Within the inner heliosphere, this interaction is largely dominated by conservation of momentum and the SIR propagates at a relatively constant speed. At farther distances, the SIR can evolve into a forward and reverse pair and the propagation becomes less straightforward. For a more thorough description of the physics involved in the evolution of HSSs and SIRs we refer to Hofmeister et al. (2022).

Due to the compression in the SIR and the high speed in the plateau, accurately forecasting the arrival of a HSS at Earth is of great importance. SIRs/HSSs are responsible for the majority of *moderate* geomagnetic storms (e.g., Echer et al., 2013; Gonzalez et al., 1999), particularly during solar minimum, when there are fewer other drivers of storms. They are also responsible for a small fraction of severe storms (e.g., Richardson et al., 2006; Zhang et al., 2007). In the case of long-lived CHs, the same HSS can drive recurrent storms over multiple solar rotations, that is, approximately every 27 days (e.g., Tsurutani et al., 2006). Gerontidou et al. (2018) estimated that, during 2009–2016, 52 geomagnetic storms (out of a total of 122) could be directly attributed to HSSs. Grandin et al. (2019) studied 588 HSSs during 1995–2017 and found that these events tend to reach their highest geoeffectiveness during the declining phases of a solar cycle, noting however that there may be cycle-dependent differences—for example, Solar Cycle 24 generally featured less geoeffective HSSs than Solar Cycle 23 did. From these statistical results, it is clear that HSSs play a valuable role in driving space weather effects at Earth. However, Gressl et al. (2014) reported that predicted HSS arrival times tend to be associated with uncertainties of the order of 1 day, and Jian et al. (2011) found that HSS forecasts can be off by up to 2 days at 1 au and up to 4 days at 5 au. Additionally, Riley et al. (2012) remarked that models can reproduce poorly the overall structure of the ambient solar wind even for solar minimum periods, when the heliospheric conditions are expected to be less complex.

HSSs are typically modeled via either fluid or magnetohydrodynamic (MHD) simulations (e.g., Odstrcil, 2003; Owens et al., 2020; Pomoell & Poedts, 2018; van der Holst et al., 2010). For these models, the inner boundary (often at 0.1 au) must be specified. This is typically done using a (photospheric) magnetogram to derive a solution for the coronal magnetic field, then applying a coronal model (e.g., Arge et al., 2004; Mikić et al., 1999; Pinto & Rouillard, 2017; van der Holst et al., 2014) to propagate the plasma properties up to the inner boundary. Beyond this, the model is physics-driven, solving differential equations to simulate both its temporal and spatial evolution. While somewhat computationally expensive, these models are currently run for real time forecasts, such as at NOAA's Space Weather Prediction Center (SWPC; https://www.swpc.noaa.gov) and at the UK Met Office (https://www.metoffice.gov.uk/weather/specialist-forecasts/space-weather). International efforts aimed at unifying the validation of ambient solar wind models are currently underway (e.g., Jian et al., 2015; Reiss et al., 2022).

While important in its own right, accurately modeling the solar wind—including any HSS—is critical for successfully capturing the interplanetary evolution of coronal mass ejections (CMEs; e.g., Webb & Howard, 2012). CMEs, entangled structures of plasma and magnetic field, routinely erupt from the Sun and can drive significant space weather effects at Earth and throughout the solar system (e.g., Pulkkinen, 2007; Temmer, 2021). Many of the most severe space weather events result from the interaction of a CME with a HSS. In fact, two of the three strongest geomagnetic storms of Solar Cycle 24 (in terms of the Dst index) were due to a CME immediately followed by a HSS. These are the 17 March 2015 storm, strongest of the cycle with the Dst index reaching −234 nT (e.g., Kataoka et al., 2015), and the 26 August 2018 storm, third-strongest of the cycle with the Dst index reaching −175 nT (e.g., Palmerio et al., 2022). The second-strongest storm, on 23 June 2015 and with the Dst index reaching −198 nT, on the other hand, was driven by successive, interacting CMEs (e.g., Augusto et al., 2018). In the CME-followed-by-HSS scenario, the fast solar wind that trails a CME compresses the material ahead of it, thus inhibiting (or at least lessening) expansion—this means that a CME is more likely to maintain high speeds, enhanced densities, and strong out-of-ecliptic fields. Another possible CME–HSS interaction scenario, albeit rarer, is encountered when a CME is entirely embedded within a fast solar wind stream (e.g., Heinemann et al., 2019), in which the speed of the CME is expected to eventually match the bulk speed of the HSS.

The space weather modeling of CMEs is typically limited to simple arrival time models (e.g., Kay & Nieves-Chinchilla, 2021; Mays et al., 2015; Riley & Ben-Nun, 2022; Vršnak et al., 2013), even in operational settings (e.g., Pizzo et al., 2011). In the simplest models, a one-dimensional drag is calculated between a CME and the background solar wind, which determines how the CME's speed changes as it propagates, ultimately determining the arrival time. While MHD models usually assume a structured solar wind, in the case of analytical models a constant background without any HSS is typically used. Recently, Kay, Nieves-Chinchilla, et al. (2022) incorporated the ability to include a static HSS within ANTEATR, an analytical interplanetary CME model. Kay, Nieves-Chinchilla, et al. (2022) showed that the interaction between a HSS and CME can decrease the CME's transit time by 10 hr and has significant effects on its velocity and the compression of the magnetic field in the CME-driven sheath, critical factors for predicting the severity of any resulting geomagnetic storm. We note that the interaction between a CME and HSS can be simulated in fluid simulations by treating the CME as a pressure pulse, but the results contain little to no information about the magnetic field and there is only time for a limited number of runs in a real time scenario. More sophisticated MHD simulations that treat CMEs as fully magnetized structures (e.g., Jin et al., 2017; Maharana et al., 2022; Török et al., 2018; Verbeke et al., 2019) cannot currently be used for forecasts due to computational limitations.

In this work, we present a new solar wind model—the Mostly Empirical Operational Wind with a High Speed Stream (MEOW-HiSS) model. MEOW-HiSS is simply a collection of empirical fits to a time-dependent MHD simulation of a HSS. MEOW-HiSS has been designed for efficiency and can nearly instantaneously generate time-dependent HSS profiles, which is ideal for coupling to simple interplanetary CME models or even for forecasting the solar wind itself. Section 2 describes how we define MEOW-HiSS from the MHD simulations. Section 4 quantifies how well the model reproduces the MHD results and Section 5 shows how the model can be extended to two-dimensions. In Section 6, we present MEOW-HiSS as a standalone tool for in situ HSS forecasts. We present a method for determining its input from remote observations and quantify how well it works for four HSS observed at 1 au.

2. MEOW-HiSS

2.1. MHD Simulations

We base MEOW-HiSS on a set of 3D MHD simulations performed by Hofmeister et al. (2020) using the European Heliospheric Forecasting Information Asset (EUHFORIA; Pomoell & Poedts, 2018). In these simulations, a circular CH is placed at the solar equator at the base of the corona and a constant expansion factor of one is assumed up to the inner boundary of the model's coronal domain, set at 0.1 au. Within the region of the inner boundary corresponding to the CH, there are a uniform speed of 650 km/s and a proton density of 150 cm^{-3}. Outside the CH region, there are slow solar wind values of 350 km/s and 500 cm^{-3}. Both the CH and ambient solar wind regions have their gas pressure set to 3.3 nPa and magnetic field strength set to 217 nT. Once the inner boundary is specified, the solution relaxes for 17 days, yielding a steady-state rotating HSS within the ambient solar wind. The area of the CH can be varied, with larger CH are as producing faster HSS. For more details on the MHD simulations of the idealized CHs, see Hofmeister et al. (2020).

Within this set, we identify different MHD simulations using two parameters—the area of the CH and the distance of the front of the HSS from the Sun. Our set contains results for 17 CH areas between 5×10^9 and 2.5×10^{11} km^2. For a given CH area and time step, we extract a radial profile from the inner boundary of 0.1 au to the outer boundary at 1.2 au. We extract this profile at a fixed location corresponding to the intersection of the equator and the central meridian. As the Sun rotates, the CH moves past the central meridian and the HSS propagates out radially. We repeat the extraction process for each time step at which some portion of the HSS is within the simulation domain. The process is then repeated for all CH areas. We sample radial profiles from the MHD results at hourly resolution, yielding 110–160 different time steps for each CH area, with the larger areas having fewer steps as their associated HSSs propagate through the simulation domain more quickly than those from smaller CH areas. For each time and CH area, we extract the radial velocity (v_r), number density (n), radial magnetic field (B_r), longitudinal magnetic field (B_{lon}), temperature (T), and longitudinal velocity (v_{lon}) as a function of radial distance (r).

2.2. MEOW-HiSS General Derivation

Here, we outline the general procedure used to derive MEOW-HiSS. MEOW-HiSS can be thought of as a pair of layered regressions that constrain a set of simple functions that mimic the shape of an MHD profile. For each

MHD parameter, this set of simple functions is predetermined and is the same for all CH areas and time steps, but the constraining values vary from case to case. We start with a very general outline to provide the big picture, then provide more details in Section 2.4. An explicit example showing the process using the actual MHD results is shown in Supporting Information S1.

Figure 1 shows a graphic visualization of the process used to develop MEOW-HiSS. To perform this analysis, we work with the plasma parameters (n, v_r, B_r, B_{lon}, T) from an MHD HSS profile normalized by the corresponding values in an ambient simulation. This removes the radial variations, such as n generally falling as the square of the distance, and keeps the magnitude of the profiles between about zero and two. The longitudinal velocity cannot be normalized as such because the ambient value is zero so we perform that analysis in physical units. We illustrate the process for a generic parameter "y" representing any of the normalized plasma parameters or the unnormalized longitudinal velocity.

We begin with the set of all the MHD profiles of y, represented by the gray box in Figure 1. Within the "All MHD results" region, each color represents a different CH area, and each CH area has multiple profiles in it corresponding to different time steps of the MHD simulation. We take a single CH area, represented by the blue box, and from that pull a single profile. This profile shows the variation of y versus heliocentric distance, r, at one specific time step.

The first step is to split the profile of $y(r)$ into small segments with simple behavior that can be described using basic mathematical functions. To do this, we start with boundaries with physical interpretations. We provide details about these specific boundaries in Section 2.4. For this overview, it is sufficient to know that these boundaries split the profile into regions with "nice" segments. The different regions are shown with different shading, alternating blue and orange, in step 1 of Figure 1. We label the boundaries as x_i the farthest points having the lowest values of i as they would be first observed in situ. The front of the HSS is labeled as simply $\mathbf{X}$. We record $\mathbf{X}$ and the x_is for this time step.

The next step is to assign a type of simple mathematical function to each segment. We consider five types, a constant or flat segment, a line, an exponent, a sine, and an adjusted sine. Figure 2 shows examples of these segments, which we describe in more detail in Section 2.4. In the example shown in step 2 of Figure 1, the fuzzy red line represents the set of these segments. From right to left we start with a flat segment, followed by three linear segments, and another flat segment. We note that this illustrative example is much simpler than the complexity required for the actual MHD profiles.

We then determine what values of y are needed to constrain each segment. Assuming y is a normalized parameter, then in our example the flat parts are known to be 1, and we only need two values, y_1 and y_2, to generate the full empirical profile. These points are represented by blue dots in step 3 within Figure 1. The linear segments run from ($\mathbf{X}$,1) to (x_1, y_1), from (x_1, y_1) to (x_2, y_2), and from (x_2, y_2) to (x_3, 1). We record the values of y_1 and y_2.

For this CH area and time step, we now have a set of x values, representing the location of the boundaries, and a set of y values, representing the magnitude at critical constraining points. In Figure 1 these are represented with a white circle. Steps 1–3 are repeated for each time step, converting the profiles into the sets of [x] and [y] as illustrated in step 4. If there are 100 time steps for the blue CH area used as an example, we will now have 100 sets of [x] and [y].

We then fit $\mathbf{X}$ as a function of time using the known time step of each profile. The relative MHD time is important (e.g., the difference between some t_1 and t_2 is an hour) but the absolute time (e.g., $t_1 = 42.3$ hr) has less significance outside of the MHD simulation. We find a linear relation between $\mathbf{X}$ and t is appropriate, suggesting that $\mathbf{X}$ moves out radially at roughly constant speed within the MHD simulation domain. We can also invert $\mathbf{X}(t)$ to get the arbitrary MHD time as a function of HSS front distance. We record the two coefficients that determine $\mathbf{X}(t)$.

From here, we distinguish each MHD time step by its value of $\mathbf{X}$ instead of the arbitrary MHD time. We take the sets of boundary locations, [x], and fit each x_i as a function of $\mathbf{X}$ (e.g., $x_1 = C_{x10} + C_{x11}\mathbf{X}$). In most cases a linear relationship is sufficient, but, for a few x_i, third order polynomials are needed. We record the two or three coefficients (C_x's) needed to reconstruct each $x_i(\mathbf{X})$. In step 5 in Figure 1, we represent the full set of all C_x's for all x_i as [$x(\mathbf{X})$]. We repeat the same procedure for the constraining values y_i to get a set of coefficients [$y(\mathbf{X})$]. The fits to $y_i(\mathbf{X})$ tend to require third or fourth order polynomials. The supplementary material shows specific examples of fitting the boundaries and constraining values as functions of the front distance.

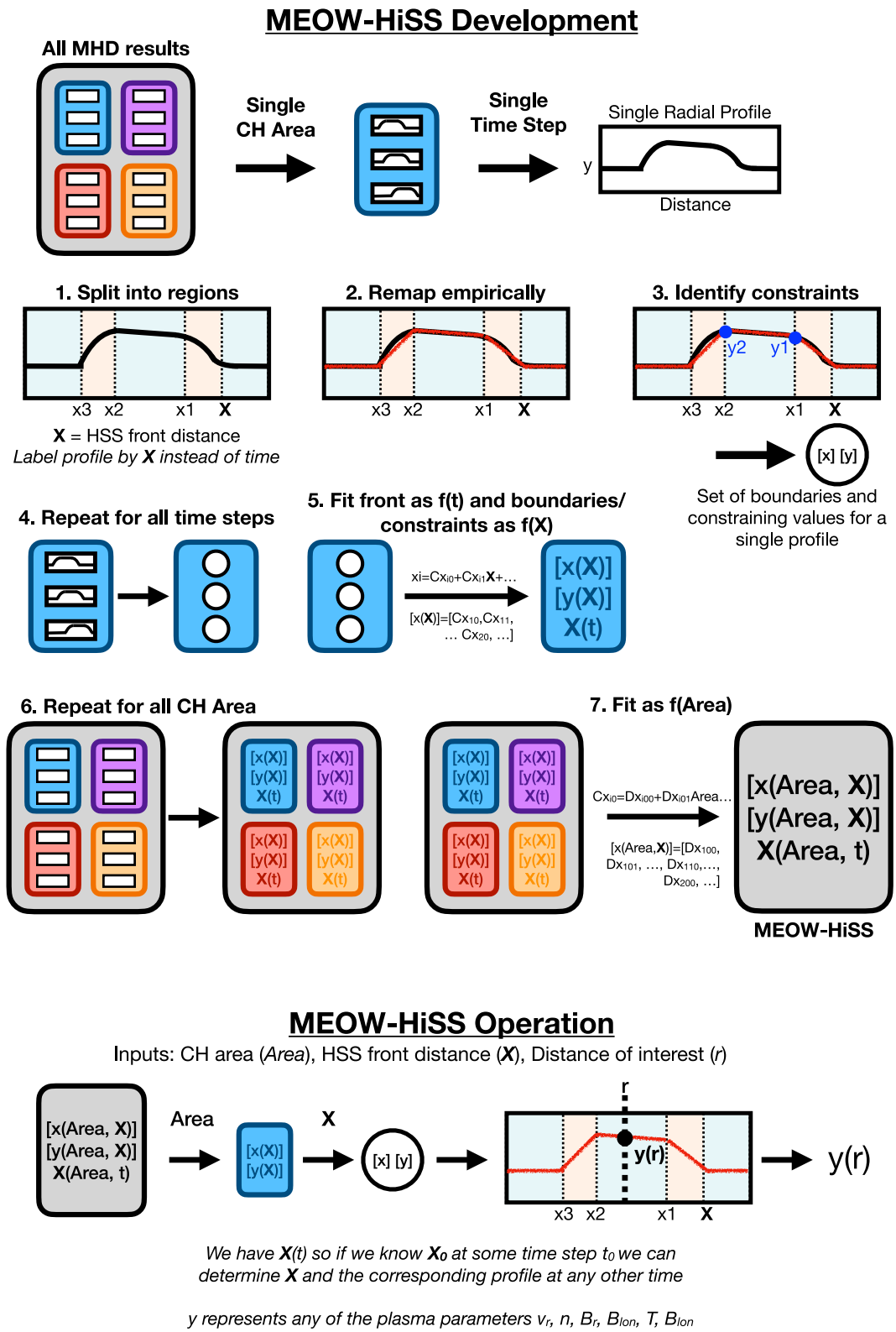

Figure 1. Cartoon illustration of the procedure used to develop the MEOW-HiSS model (top) and how the model operates in practice (bottom).

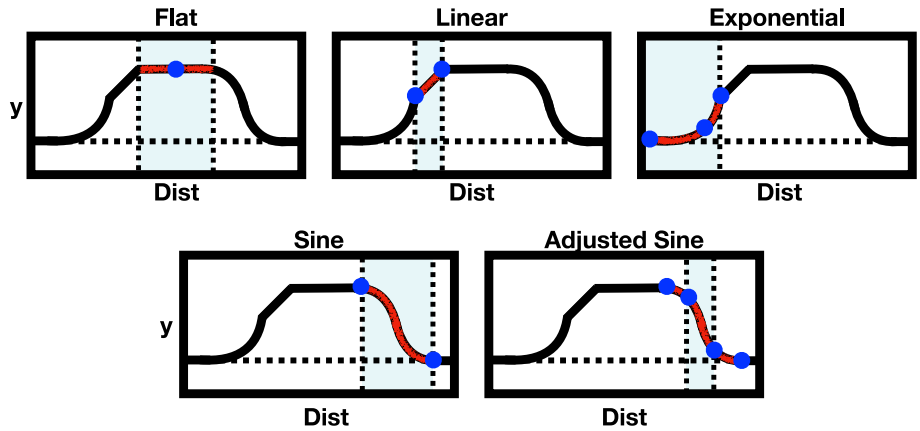

Figure 2. Cartoon illustrating the five different types of empirical functions used to reconstruct the magnetohydrodynamic profiles.

We then repeat steps 1–5 for all the different CH areas. This is represented in step 6 with the profiles becoming $[x(\mathbf{X})]$, $[y(\mathbf{X})]$, and $\mathbf{x}(t)$ for each different color/different CH area region. The exact same boundaries, mathematical segments, and constraining values are used across all CH areas so we have the same collection of C's for each area, but each with their own unique values. In other words, for example, we now have the first order coefficient for the linear fit to $x_1(\mathbf{X})$ for each of the CH areas. We then apply one final regression to determine how each C varies with CH area. These regressions tend to use second or third order polynomials, which produces a new set of coefficients, labeled as D's in step 7 of Figure 1. The set of all coefficients from all these final regression are referred to as $[x(\text{Area},\mathbf{X})]$, $[y(\text{Area},\mathbf{X})]$, and $\mathbf{X}(\text{Area},t)$ in step 7 of Figure 1. These coefficients and the set of simple functions used in step 2 are the entire basis of MEOW-HiSS.

2.3. MEOW-HiSS Usage

The derivation of MEOW-HiSS is essentially just regressions of regressions, but the structure of MEOW-HiSS is more easily understood with an example of its usage, which we represent in the bottom of Figure 1. We start with the gray region on the left representing the collection of all of the coefficients. MEOW-HiSS first uses the input CH area to downselect to a specific set of coefficients for that area, which is represented by selecting the blue box in Figure 1. Mathematically, MEOW-HiSS uses the D coefficients to generate the appropriate C coefficients for this area.

Next, MEOW-HiSS uses the front distance and the C coefficients to determine the appropriate constraining values $[x]$ and $[y]$. Finally, it determines which region the input distance of interest fall within using the x_i in $[x]$. In Figure 1 this is represent as r falling in the middle region between x_1 and x_2. MEOW-HiSS then uses the appropriate simple function and corresponding constraints to determine the precise value of y at r. In this example, this corresponds to a linear profile constrained by y_1 and y_2.

MEOW-HiSS also simulates time-dependent profiles. If we know the front distance at some time t_1' we can invert $\mathbf{X}(t)$ to determine the corresponding MHD time t_1. Relative time is the same between the MHD and any other domain. If we wish to find a profile at some subsequent time t_2' then we simply determine $\mathbf{X}(t_1 + (t_2' - t_1'))$. The new front distance fully determines the profiles at the subsequent time.

2.4. Derivation Details

In this section we provide a few additional details on the different simple functions we use and the criteria used to select the region boundaries. Further information, including a full example of the fitting procedure, can be found in Supporting Information S1.

2.4.1. Simple Functions

Figure 2 shows examples of the five different simple functions we use to reconstruct the MHD profiles. We show an illustrative profile in black and each simple function is shown in red. The blue shaded region highlights the

segment we are trying to reconstruct in each scenario. The blue dots show the points that are needed to constrain each option.

The first option is a flat segment (top left panel), which is constrained by a single value. The second option is a linear segment (top row, middle panel), which requires two constraining values. In most cases we take these constraining values at the boundaries of the region, but interior values can also be used. The third option is an exponential segment (top right panel), which requires three constraining values. One of these represents the tail of the exponent, setting the limit it approaches in that direction (leftmost blue dot in this panel). The other two points set the rate of the exponential increase in the other direction.

The last two options are sinusoidal segments. The first of these is a simple half period of a sine wave. This option is constrained by the values at the boundaries, which represent the minimum and maximum values (i.e., the amplitude). The period is determined by the width of the region. In some cases, we may not want to describe a region using the full amplitude and a half-period of a sine function. For this we use an adjusted sine wave, which has smaller amplitude and less than a half period. It can be adjusted on one or both sides. Using the cartoon example, we have four constraining points as both sides are adjusted. For the left side of the segment we have the value at the left boundary and also the value/location where the sine reaches its maximum value. The same is true on the right side for the minimum value. These exterior points set the actual period and amplitude of the sine segment.

In practice, we often do not actually have the exact location of the exterior points but we do know the magnitude they should reach on each side. In other words, we know the y values of the exterior dots in Figure 2 but not their distance. However, the full amplitude combined with the values at the boundaries is sufficient to determine the location of the exterior points. For such cases, we let the adjusted sinusoidal segment extend beyond the selected region until it reaches the calculated distance of the exterior points.

We note that combining these individual segments results in a profile that is mathematically continuous but not smooth. There are no jumps in the plasma properties at the boundaries, but there will be discontinuities in the gradient of the profile. We have picked segments that mostly appear visually smooth, which should minimize the extent of the gaps at the discontinuities in the gradient, but they will exist. We make no use of the gradient in this work so the visually smooth profiles are sufficient, but acknowledge the lack of mathematical smoothness.

2.4.2. Boundaries

As mentioned, we split the profiles into regions using a systematic set of boundaries. We first select boundaries that divide the profile based upon the different components of the HSS (SIR, plateau, tail). The SIR shows the most structure so we split it into three sections distinct segments. This yields 5 regions corresponding to the full HSS structure, as well as upstream and downstream ambient regions. The six boundaries, their physical interpretation, and numerical definition are as follows.

- x_1—Upstream ambient/SIR boundary—where change in n and B_r first exceeds 20% of the maximum change
- x_2—Peak in SIR flow on ambient solar wind side, most positive v_{lon}
- x_3—HSS front, defined where v_{lon} changes sign
- x_4—SIR/plateau boundary, most negative v_{lon}
- x_5—Plateau/tail boundary, where v_r first falls below value at x_4
- x_6—Tail/downstream ambient boundary, where the change in v_r reaches 5% of the total $\Delta v_r/v_{r0}$.

Note that the broad overview in Section 2.2 contained several simplifications compared to the rigorous process. First, we can not fully consider a single plasma parameter at a time since the definition of the boundaries depends on a combination of parameters. Once the boundaries are determined, the rest of the regression process does proceed separately for each individual parameter. Second, we labeled the first/rightmost point as the HSS front **X** in the cartoon. Using the traditional definition of the front at the location where the lateral flow reverse direction (e.g., Belcher & Davis, 1971; Richardson et al., 1996), **X** is actually equivalent to x_3.

In some cases, additional boundaries are required to split the MHD profile into nice segments that can be mimicked with the simple mathematical functions. These additional boundaries can all be estimated from the x_1–x_6 values, but are simply mathematically convenient locations rather corresponding to physical boundaries between structures. These points are

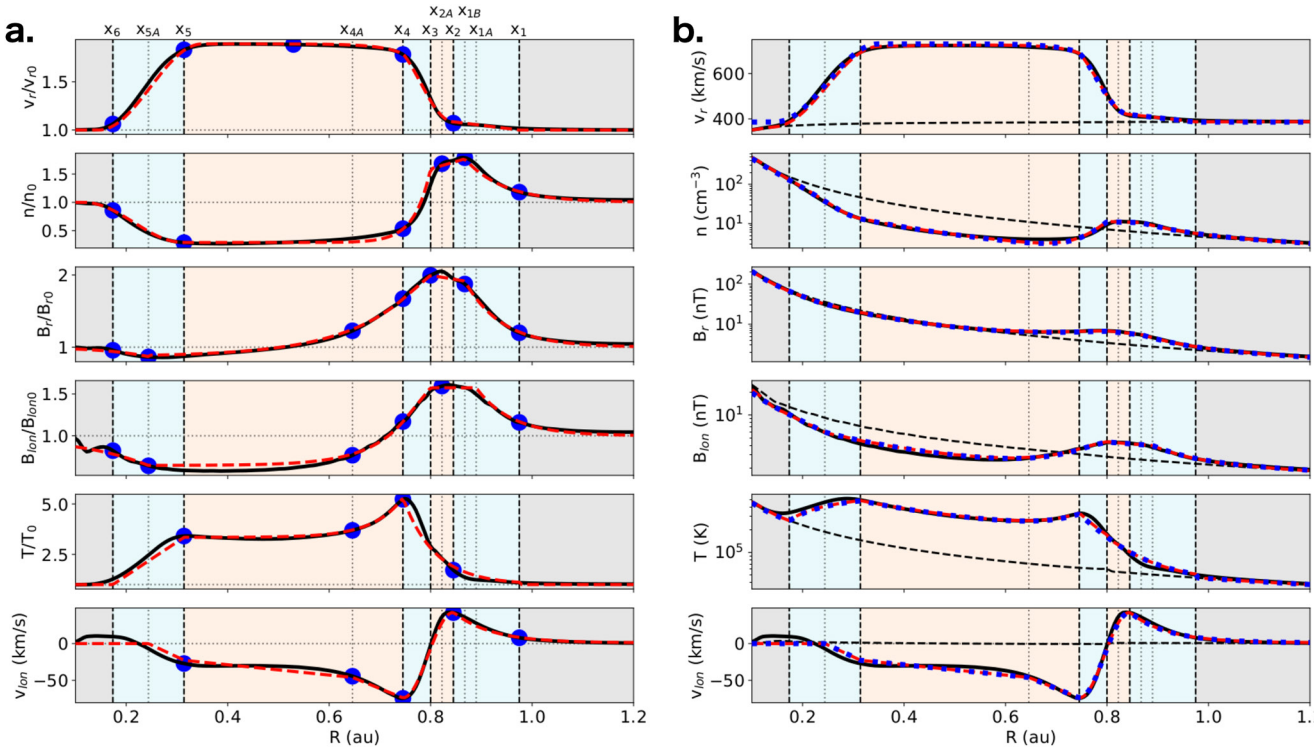

Figure 3. Comparison between magnetohydrodynamic (MHD) results and the MEOW-HiSS model for an 8×10^{10} km^2 area CH with the high speed stream front at 0.8 au. Panel (a) shows results normalized by the ambient solar wind model and panel (b) shows unscaled results in physical units. In both panels the solid black line shows results from the MHD model and the dashed red line shows results from MEOW-HiSS. The blue dots in panel (a) represent locations used to constrain the empirical functions and the region boundaries are labeled at the top. In panel (b) the dashed red lines correspond to the unscaled MEOW-HiSS results using a MHD ambient profile, whereas the dashed blue lines use an analytical ambient profile. The dashed black line shows the MHD ambient profile.

- $x_{1A} = x_2 + (x_2 - x_3)$
- $x_{1B} = 0.5 \cdot (x_{1A} + x_2)$
- $x_{2A} = 0.5 \cdot (x_2 + x_3)$
- $x_{4A} = x_4 - (x_2 - x_4)$
- $x_{5A} = 0.5 \cdot (x_5 + x_6)$,

where the numeric subscript indicates which physical boundary location it follows. The letter distinguishes between multiple mathematical boundaries following the same physical one (i.e., 1A and 1B both follow 1). Not all boundaries are used for all plasma parameters.

2.4.3. Further Details

Figure 3 shows results for a profile from a 8×10^{10} km^2 area CH with a HSS front distance of 0.8 au. We show the MHD profile in black and the MEOW-HiSS result with a dashed red line. The vertical dashed lines show the calculated boundaries, both the physical and mathematical ones, with labels at the top. The shading shows the different physical regions. Starting at the farthest distances we have the upstream ambient region (gray), three regions for the SIR (blue, orange, blue), the plateau (orange), the tail (blue), and the downstream ambient region (gray). From top to bottom the panels show the velocity, number density, radial magnetic field, longitudinal magnetic field, temperature, and longitudinal velocity. Panel (a) shows all values (except for v_{lon}) normalized by the ambient MHD profile. The dotted line represents a value of 1, meaning a match between the HSS and ambient results. Panel (b) shows the results in physical units to show the radial variations. The dashed line in (b) shows the ambient MHD profile that is used for normalization.

The blue dots in Figure 3a show the constraining values each profile. The details of the specific functions and constraining values are shown in Table 1. Within a column, rows from top to bottom show details from upstream to downstream. The leftmost columns identify the corresponding physical features and the region boundaries in terms of specific x values. The remaining six columns contain details for the empirical representation of each

Table 1
MEOW-HiSS Empirical Set Up

Feature	Region	v_r/v_{r0}	n/n_0	B_r/B_{r0}	B_{lon}/B_{lon0}	T/T_0	v_{lon}
Upstream	Up → 1	**Flat** 1	**Exp** 1, x_1, x_{1B}	**Exp** 1, x_1, x_{1B}	**Exp** 1, x_1, x_{1A}*	**Flat** 1	**Exp** 1, x_1, x_2
SIR	1 → 1A	**Lin** 1, x_2				**Exp** 1, x_2, x_4*	
	1A → 1B				**Flat** Max		
	1B → 2		**Lin** x_{1B}, x_{2A}	**Lin** x_{1B}, x_3			
	2 → 3	**Sin** x_2, x_4 (Max)					**Sin** x_2, x_4
	3 → 4		**Exp** x_3*, x_4, x5	**Lin** x_3, x_4	**Lin** x_3, x_4		
Plateau	4 → 4A	**Exp** x_2*, x_4, Max		**Exp** x_4, x_{4A}, x5A	**Exp** x_4, x_{4A}, x5A	**Exp** x_4*, x_{4A}, x5	**Lin** x_4, x_{4A}
	4A → 5	**Flat/Sin** Max					**Lin** x_{4A}, x_5
Tail	5 → 5A	**Sin** (Max) x_5, x_6 (1)	**Sin** x_5, x_6 (1)			**Lin** x_5, 1	**Lin** x_5, 1
	5A → 6			**Exp** x_{5A}, x_6, 1	**Exp** x_{5A}, x_6, 1		**Flat** 1
Downstream	6 → Down	**Sin/Flat** 1	**Sin/Flat** 1			**Flat** 1	

plasma parameter. The cells represent individual segments, the simple function used within that segment is first listed in bold, followed by the locations of the constraining points. For the exponential segments the underlined value represents the tail of the exponent. For the sine segments, additional parameters in parenthesis indicate that it is an adjusted sine on one or more sides. A parenthesized number on the left indicates an adjustment on the upstream side and right on the downstream side. In cases where we extend the adjusted sine segments to whatever location they reach that minimum or maximum value we include "Sin" in the label of the preceding or trailing segment. Numbers with asterisks indicate some subtle detail, which we explain in Supporting Information S1.

As an example of reading the shorthand within Table 1, we describe the segments used in the velocity profile. The remaining parameters are fully described in Supporting Information S1. We start upstream with a flat profile at a value of 1. Once we reach x_1 the profile changes to a linear profile varying between 1 at x_1 and y_2 at x_2, where y_2 is found from the regressions we described in Section 2.2. Between x_2 and x_4 we use a sine segment that has been adjusted on the downstream side to reach the overall maximum in v (also found from the regressions) at some distance beyond x_4. Between x_4 and x_{4A} we use the tail of an exponent. This exponent has a tail at the maximum v, and is further constrained by the value at x_4, and an assumption of a value of 1 at x_2. Between most of x_{4A} and x_5 we use a flat segment at the maximum in v. Between x_5 and x_6 we use a sine segment that is adjusted on both sides (to the maximum on the upstream side and to 1 on the downstream side). In the downstream region we finally return to a flat value of 1. In both x_{4A} to x_5 and beyond x_6, we extend the adjusted sine segment to reach its full amplitude.

Looking at Figure 3 we see that MEOW-HiSS generally does a good job of reproducing the MHD results, we will describe this more quantitatively in later sections. This general math is true for both the scaled and unscaled values (panels a and b). In Figure 3b, the dashed red line shows MEOW-HiSS results using the ambient MHD profile to convert from scaled to unscaled values. Alternatively, we can use a simple analytic model for the ambient solar wind. In this ambient model the velocity remains constant, the density falls as the distance-squared, the magnetic field follows a Parker spiral, the temperature has a power law dependence, and there is no longitudinal flow. We tune the analytic model to match the MHD results at 1 au. The dashed blue line shows the unscaled MEOW-HiSS results using the tuned analytic ambient model. These results are largely indistinguishable from the MEOW-HiSS results using the ambient MHD profile.

2.5. Computational Efficiency and Domain

The primary purpose of MEOW-HiSS is to provide a computationally efficient, time-dependent HSS background, which is the reason why we have forsaken nearly all physics in favor of simple equations. Here we quantify the efficiency of MEOW-HiSS.

The model was developed on an off-the-shelf 2015 Macbook Pro and runs in Python 3 with no explicit parallelization. We perform a speed test by calculating the solar wind parameters at a million different points. We establish a HSS by providing the CH area and initial HSS front distance. We then randomly select a million different

combinations of positions and times within the range appropriate for this HSS. Simply calculating the normalized HSS values takes a total of 1.75 min. Scaling these to physical units requires specifying an ambient background profile. If we read in an ambient profile from the MHD results, which we then reproduce with splines, and use this to denormalize, the process takes a total of 3.5 min. Alternatively, if we use the tuned analytic ambient background solar wind profile, the full process only takes 2 min with almost no loss in quality of results.

The original MHD profiles extend from 0.1 to 1.2 au, but, to some extent, we can produce values for when the front of the CME is beyond 1.2 au. When performing the regressions, we include any profile that contains some portion of a HSS, which includes many where the HSS front has exited the outer boundary. Our regression for x_3 as a function of time was derived from times when the HSS front was within the domain, but the regression can be used to extrapolate values to farther distances and/or later times, within reason. This allows us to make use of the many profiles that contain a large number of the points used to constrain the empirical segment but that do not explicitly include x_3. The farther x_3 propagates beyond 1.2 au, the more inaccurate our predicted position becomes (presumably), thus we caution about extrapolating to too far of distances, which we discuss further in Section 3.

3. Quantifying Quality of Fits

Before presenting any further comparison between MEOW-HiSS and MHD profiles, we define a metric for the quality of fit. This metric allows us to be quantitative when describing the ability of MEOW-HiSS to reproduce the MHD profiles, rather than relying on vague descriptions of general success. We calculate this metric for all combinations of CH area and HSS front distance within our domain. We present these results in this section to provide context for the following descriptive analysis.

We define each solar wind parameter as y_i, which is a function of the CH Area, A_{CH}, HSS front distance, $\mathbf{X}$, and the radial position within that profile, r_j. For one parameter, one CH area, A_{CH}, and one front distance, we find the mean absolute fraction error (MAFE) in that profile as

$$\mathrm{MAFE}(\mathbf{X}, A_{\mathrm{CH}}) = \frac{1}{N_r} \sum_{r_j=0.1}^{1.2} \left| \frac{y_{\mathrm{MH},i}(\mathbf{X}, A_{\mathrm{CH}}, r_j) - y_{\mathrm{MHD},i}(\mathbf{X}, A_{\mathrm{CH}}, r_j)}{y_{\mathrm{MHD},i}(\mathbf{X}, A_{\mathrm{CH}}, r_j)} \right| \tag{1}$$

where N_r is the number of radial points along the profile, and the subscripts MH and MHD designate either MEOW-HiSS or MHD values. To clarify, each combination of an individual parameter, front distance, and CH area will have its own MAFE ($\mathbf{X}$, A_{CH}). Within this work, we assume 111 points for spacing of 0.01 au along a MEOW-HiSS radial profile. We can calculate the MAFE over the full profile from 0.1 to 1.2 au, but this will overly minimize our errors by including the ambient portions. Accordingly, we calculate the MAFE for only the HSS portion of the profile (i.e., between x_1 and x_6) that falls between 0.1 and 1.2 au (where we have MHD for comparison). The MAFE then represents the average percentage error in a parameter at any point within the HSS portion of the profile.

Figure 4 shows this MAFE for 5 of the 6 plasma parameters MEOW-HiSS simulates (v_r panel (a), n (b), B_r (c), B_{lon} (d), T (e)). We do not include the MAFE for v_{lon} as it is significantly worse than every other parameter (typically by an order of magnitude) so we cannot easily show it on the same scale. We show the MAFE as a percentage rather than a decimal fraction, the color contours range between 0% and 20%. In the saturated yellow region for 20% and above, we include line contours showing increments of 10%. The darkest line indicates a value of 20% and the error increases as the lines become lighter gray. The lines are labeled in the temperature panel as an example but labels are not included in other panels for reasons of clarity. We sample the full range of CH areas for which we have MHD profiles and use front distances up to 2 au, using estimates for $\mathbf{X}$ beyond 1.2 au. The black region in the corner of Figure 4 corresponds to cases where there is no longer a portion of the HSS within the MHD simulation domain (i.e., a small HSS at too far of a distance such that $x_6 > 1.2$ au).

MEOW-HiSS reproduces v_r within less than 5% MAFE for nearly the full range of distances and areas. We see a slight increase in the error toward large areas and far distances but we only exceed an error of 20% in the far corner of parameter space. We see similar behavior for both magnetic field MAFE, though the error is slightly higher than seen for v_r. Most of this parameter space has a MAFE less than 10% for both B_r and B_{lon} but once the distance goes beyond 1.5 au the MAFE begins to rapidly increase. The number density and temperature have higher MAFEs than the magnetic field, with the temperature being worse than the density, but exhibit the same general behavior of the MAFE rapidly increasing with distance beyond about 1–1.5 au.

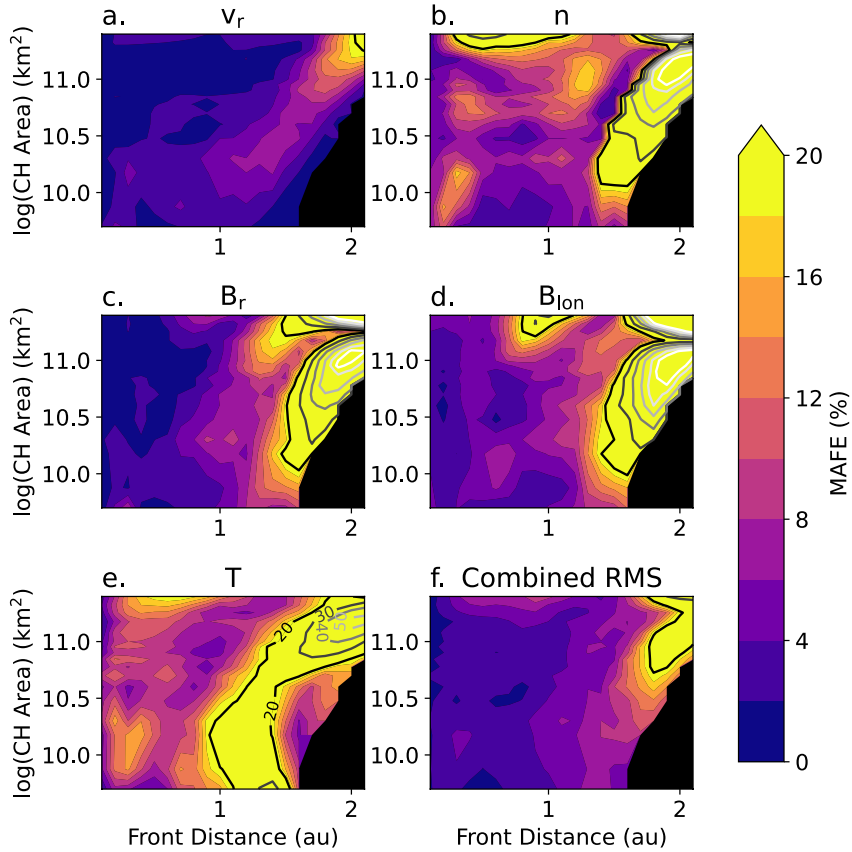

Figure 4. Contours showing the mean absolute fraction error (MAFE) for v_r (a), n (b), B_r (c), B_{lon} (d), T (e), and the root mean square of all five combined into a single measure (f). The color contours show variations in the MAFE between 0% and 20% and the line contours show increments of 10% starting with 20%.

As we have stated, generating MEOW-HiSS results beyond 1.2 au requires some level of extrapolation. We can only directly measure the front distance up to 1.2 au, but the regressions show that its behavior is fairly well-described by a constant velocity/linear fit (see Figure S1 in Supporting Information S1). The increase in error beyond 1.2 au is more largely driven by our ability to measure the constraining values as the front portions of the HSS begins to exit the MHD domain. For example, many of the parameters use an exponential segment between x_4 and x_5 with constraining values at x_4 and x_{4A}. We can only measure the values at x_4 and x_{4A} until they reach a distance of 1.2 au (at which time the front will be slightly beyond 1.2 au) but we need an estimate of these values until x_5 exits the simulation domain (at which time the front is significantly beyond 1.2 au). Using our regressions, we can safely extrapolate values at x_4 and x_{4A} for a short range beyond 1.2 au but we quickly start introducing massive errors due to the lack of constraints at farther distances.

MEOW-HiSS has some safeguards built in to decrease such errors, for example, instead of using the exponential profile we established in the "optimized" algorithm, we can simplify and use a linear profile between x_5 and x_{4A} if we cannot safely reconstruct the value at x_4. The contours in Figure 4 show that the MAFE is lowest when we can apply the full optimized algorithm (fronts below 1.2 au) and starts to increase as we are forced to use simplified structures. Eventually we reach the farthest distances where we are trying to compare just the small portion of the tail that remains within the MHD domain using a single, poorly constrained value, which is where the MAFE reach their highest values.

While the most obvious variations in MAFE over parameter space occur with respect to the front distance, we do see variation with CH area. In particular, the MAFE shows the MEOW-HiSS algorithm begins to break down toward larger areas. The largest area CHs produce HSSs that are about 1 au in duration, meaning there are very few time steps that include the full HSS within the domain. This means fewer points used in each regression and a decrease in the quality of the MEOW-HiSS results for the most extreme areas. We have also tried to pick

segments and boundaries that work well for all areas, but in some situations this is not possible. We tend to tune things toward the middle CH areas, as this will then be the best for the most cases. This increases the errors toward both limits of CH area, but the small CH area cases are more ambient-like to begin with, so the errors are more noticeable for the largest CH areas. This results in the yellow regions seen for large areas around a distance of 1 au, particularly noticeable for B_{lon} and n.

Figure 4f shows the root mean square of the MAFE (rmsMAFE) shown in each of the other 5 panels. This gives a single metric we can use to describe the quality of fit of the full simulation. We see that the rmsMAFE is below 4% for all areas as long as the front distance is ≤1 au. As the distance increases, so does the rmsMAFE, though it remains below 10% up to about 1.5 au. Beyond 1.5 au it begins increasing more rapidly, reaching values greater than 20%. We conclude that MEOW-HiSS can reproduce the MHD results within about 10% accuracy or less for front distances out to 1.5 au, but caution using it beyond this distance. We have also ignored the longitudinal velocity in this error analysis and suggest that it is not particularly reliable (MAFE 20%–200%) as we will show in the individual examples in Section 4.

As an interesting quantification of the usefulness of a simple HSS model, we can calculate the rmsMAFE one would obtain if they just use an ambient solar wind profile instead of including any HSS. The results in Figure 4 show that each CH area has an average rmsMAFE around 5% across all front distances less than 1.5 au. If we calculate an analogous rmsMAFE between an ambient MHD profile and one containing a HSS, the rmsMAFE varies between 35% and 50% depending on the CH size. We conclude that even a simple HSS model such as MEOW-HiSS is an order of magnitude more accurate than not including any representation of the HSS.

4. Comparison of Individual Profiles MHD

This section shows examples comparing the MEOW-HiSS results with individual MHD profiles. We begin by discussing a time-independent case corresponding to a single CH area and HSS front distance. We then expand to look at other CH areas and distances and comment on time-dependent simulations.

4.1. Time-Independent Results of Different CH Areas at a Single HSS Distance

Figure 3 compares the MEOW-HiSS results (red) with the MHD profile (black) for an 8×10^{10} km^2 area CH, both scaled relative to the ambient case (a) and in physical units (b). In this case, we have provided the known distance of the HSS front at 0.8 au to MEOW-HiSS and are not simulating any evolution in time. The empirical and MHD profiles agree very well with only very minor differences. By eye, the most noticeable discrepancies are at the rise in temperature within the SIR, in the plateau for the longitudinal magnetic field, and in the longitudinal velocity near the tail and downstream regions.

We calculate the MAFEs for each parameter, which are listed in Table 2. Table 2 shows results for all of the profiles described in this section, the corresponding CH area and HSS front distances are listed at the top of each column. For the 8×10^{10} km^2 area CH at 0.8 au, we find errors of 1.2% in v_r/v_{r0}, 6.7% in n/n_0, 1.5% in B_r/B_{r0}, 5.3% in B_{lon}/B_{lon0}, 5.4% in T/T_0, and 24.1% in v_{lon}. Our error in n/n_0 is comparable to that in B_{lon}/B_{lon0} and T/T_0, suggesting that while there is no visually obvious error in the density, small errors are persistent throughout. The longitudinal flow speed has the largest error, which is primarily driven by MEOW-HiSS simulating zero flow at the very back of the tail when the MHD profile exhibits some fluctuation before returning to the ambient value. In this region, the error is 100%, which inflates the error over the full profile. If we only consider the region between x_1 and x_{5A}, the error in v_{lon} decreases to 16.9%.

Figure 3b includes results where we use the empirical ambient model to scale MEOW-HiSS to physical units (dotted blue line) rather than using the MHD ambient profile (red). If one looks closely there are minor visual differences, but overall the MAFE results are nearly identical. The largest change in the MAFEs is an increase of 0.4% in the temperature profile. For practical forecasting purposes, using a simple empirical model is likely preferable to the results of an ambient MHD model and this analysis suggests that doing so will minimally affect the quality of the MEOW-HiSS results.

This 8×10^{10} km^2 area CH falls within the middle of the range we consider. We have tuned our choices of boundaries and constraining values to work the best for the maximal number of cases, which tends to improve results near the middle of ranges, rather than near the extremes. To check these limits, we consider MEOW-HiSS profiles

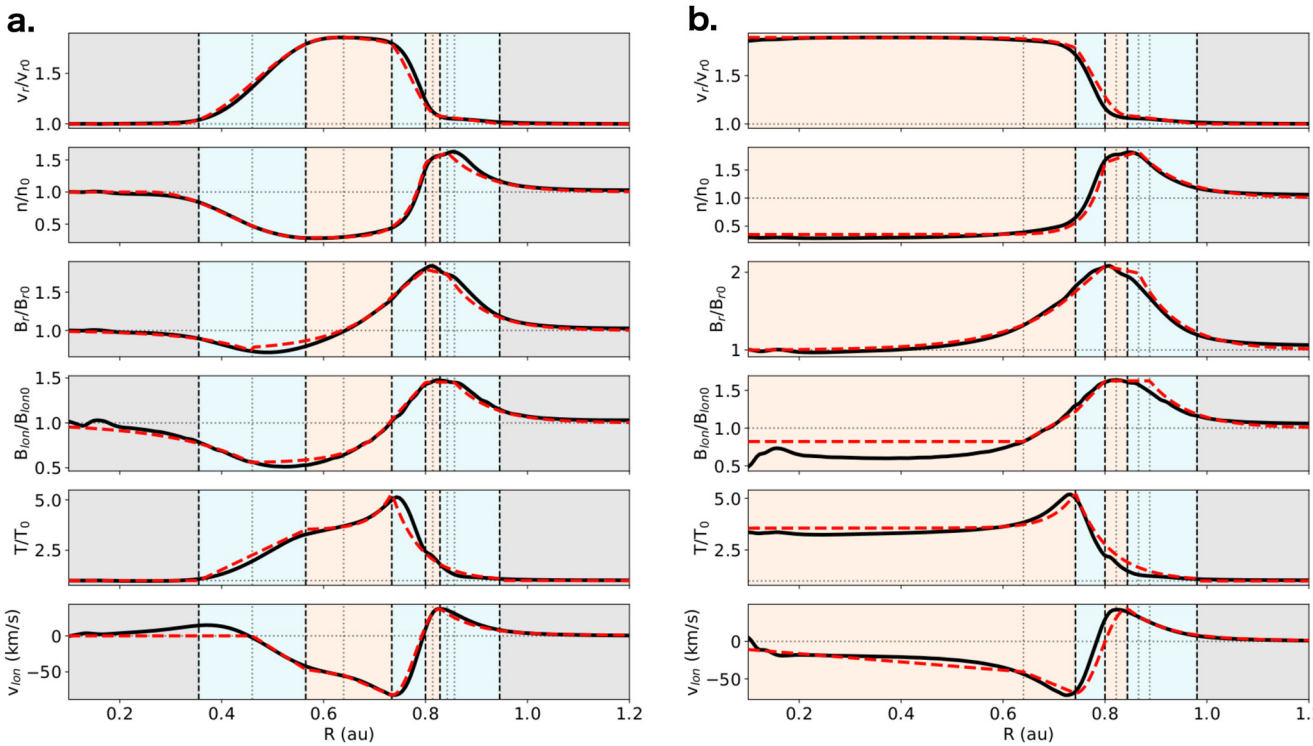

Figure 5. Same format as Figure 3a but comparing magnetohydrodynamic results (solid black line) and the MEOW-HiSS model (dashed red line) for a 3×10^{10} km^2 (a) and a 1.5×10^{11} km^2 (b) area CH. Both cases have the high speed stream front located at 0.8 au.

corresponding to CH areas of 3×10^{10} and 1.5×10^{11} km^2, shown in Figures 5a and 5b, respectively. One immediately sees that the larger CH area yields a longer duration HSS, since the case corresponding to 1.5×10^{11} km^2 extends backward beyond the inner boundary at 0.1 au. In Table 2, we see a slight increase in the MAFEs for many of the parameters, as expected.

As mentioned, the empirical functions and their boundaries were selected to accurately reconstruct the widest range of profiles possible, but we see that optimal boundaries sometimes change with more extreme CH areas. For example, the peak in n/n_0 is set at x_{1B}, which appears appropriate for the 8×10^{10} km^2 and 1.5×10^{11} km^2 areas, but the 3×10^{10} km^2 CH would be better suited with it at x_{1A}. Conversely, the break between the exponential and flat regions at x_{1A} is appropriate for the 3×10^{10} and the 8×10^{10} km^2 cases, but would be more appropriate at x_{1B} for the 1.5×10^{11} km^2 CH.

MEOW-HiSS also begins to break down for large HSSs that extend beyond the domain of the original MHD simulation, such as in Figure 5b. For example, the fit to B_{lon}/B_{lon0} is fairly poor in the plateau. When the HSS front is at this distance for this size CH, we do not have a reliable estimate of the value of B_{lon}/B_{lon0} at x_{5A}, which

Table 2
Mean Absolute Fractional Errors

CH area (10^{10} km^2)	3	3	3	8	8	8	15	15	15
HSS Front (au)	0.4	0.8	1.0	0.4	0.8	1.0	0.4	0.8	1.0
v_r/v_{r0} (%)	1.9	1.6	4.0	1.6	1.2	2.3	1.4	1.2	1.8
n/n_0 (%)	7.0	2.9	6.0	13.4	6.7	11.6	6.3	12.7	11.5
B_r/B_{r0} (%)	2.5	4.3	6.9	2.3	1.5	4.4	1.0	2.9	3.2
B_{lon}/B_{lon0} (%)	4.3	3.7	6.5	5.8	5.3	6.3	5.0	18.6	13.5
T/T_0 (%)	8.2	7.9	17.5	10.4	5.4	6.6	11.2	8.4	8.3
v_{lon} (%)	24.8	26.7	82.6	27.0	24.1	37.6	29.2	31.3	116.2

is typically used to constrain this profile within the plateau. As such, we are forced to assume the value at x_{4A} persists through the rest of the region. This is an example of the sort of safeguards built in so that MEOW-HiSS can still provide reasonable, albeit less accurate, results for as large of a range as possible.

4.2. Time-Independent Results for Additional HSS Distances

Section 4.1 showed profiles for three different size CHs, but all with the same front distance. Here we extend to different HSS front distances. Figure 6 shows results using the three CH sizes that we have considered (3×10^{10} km^2 top, 8×10^{10} km^2 middle, and 1.5×10^{11} km^2 bottom row) and for front distances of 0.4 au (left column) and 1 au (right column). Table 2 also lists the MAFEs for these cases.

For all size CHs, when the front is at 0.4 au we find that the leading portion of the HSS (SIR and front of plateau) appears to be reproduced with similar quality as for the 0.8 au case. The trailing portion near 0.1 au (back of plateau and tail), however, is typically significantly reduced in quality. As we noted earlier, as portions of the HSS extend beyond the domain of the MHD simulation the regressions begin to deteriorate, leading to either less accurate constraining values or even forcing the model to resort to a simplified description based on whatever constraining values are stable at that point. In some cases, such as for B_{lon}/B_{lon0} for the 1.5×10^{11} km^2 case, we see a slight decrease in the MAFE because the closer front distance means that we include less of a region reproduced more poorly by MEOW-HiSS, improving the overall MAFE of the region within the simulation. Overall, the profiles still shows a good visual match and the MAFEs are quite reasonable for the close front distance, with error roughly equal to or less than 10% for most parameters for all CH size cases.

For the cases with the front at 1 au, we see less variation in MAFEs relative to the 0.8 au case, particularly for the case with 1.5×10^{11} km^2 area. We note that the 1.5×10^{11} km^2 CH has generally larger MAFEs at 0.8 au than the other two sizes. It is not that MEOW-HiSS performs better for the 1.5×10^{11} km^2 case at 1 au so much as the 3×10^{10} km^2 and 8×10^{10} km^2 have caught up to the distance at which their regressions and boundary assumptions begin to break down. Still, we find that most parameters are accurate within about 5%, with a few reaching as high as 10%–20%.

We have consistently seen that the longitudinal velocity is a major exception in terms of accuracy across all CH sizes and HSS front distances. We tend to accurately reproduce the magnitude of the peaks in the flow as well as the values at the other constraining points. The exact behavior between these points is not precisely reproduced. Sometimes the MHD results display more curvature and sometimes they display less. We have not found a method that can consistently correct for this issue across all CH sizes and HSS front distances. Nevertheless, beyond identifying the location of the HSS front, the longitudinal flow velocity tends to be of less importance than the other parameters, both in terms of a background for CME propagation simulations and for space weather predictions.

4.3. Time-Dependent Results

The right column of Figure 6 shows results for when we have explicitly told MEOW-HiSS that the HSS front is at 1 au. Alternatively, we can initiate MEOW-HiSS with the front at 0.4 au and determine the full HSS profile at the time it reaches 1 au. Based on the speed of the HSS, which is set by the CH area, we determine that an 8×10^{10} km^2 case will take 48.73 hr to propagate from 0.4 au to 1 au. Setting MEOW-HiSS to generate a profile 48.73 hr later than the 0.4 au time creates a profile that is visually indistinguishable from the time-independent version shown in Figure 6. If we compare the MAFEs, the longitudinal flow error varies by 0.07% and all other parameters change by 0.01% or less. We find similar results for other size CHs. This means that MEOW-HiSS can produce time-dependent results essentially as accurately as if we explicitly provide it the HSS front distance at a given time.

5. Extrapolation to 2D

MEOW-HiSS is fundamentally a 1D model, but we can extrapolate it to 2D using the solar rotation rate. If we assume a 24.5-day rotation period at the solar equator, then a change of one degree in longitude is roughly equivalent to a time change of 1.6 hr. We can establish a HSS along a radial line at one longitude and then extrapolate it to other longitudes using MEOW-HiSS's time-dependency. Figure 7 presents an example of this concept,

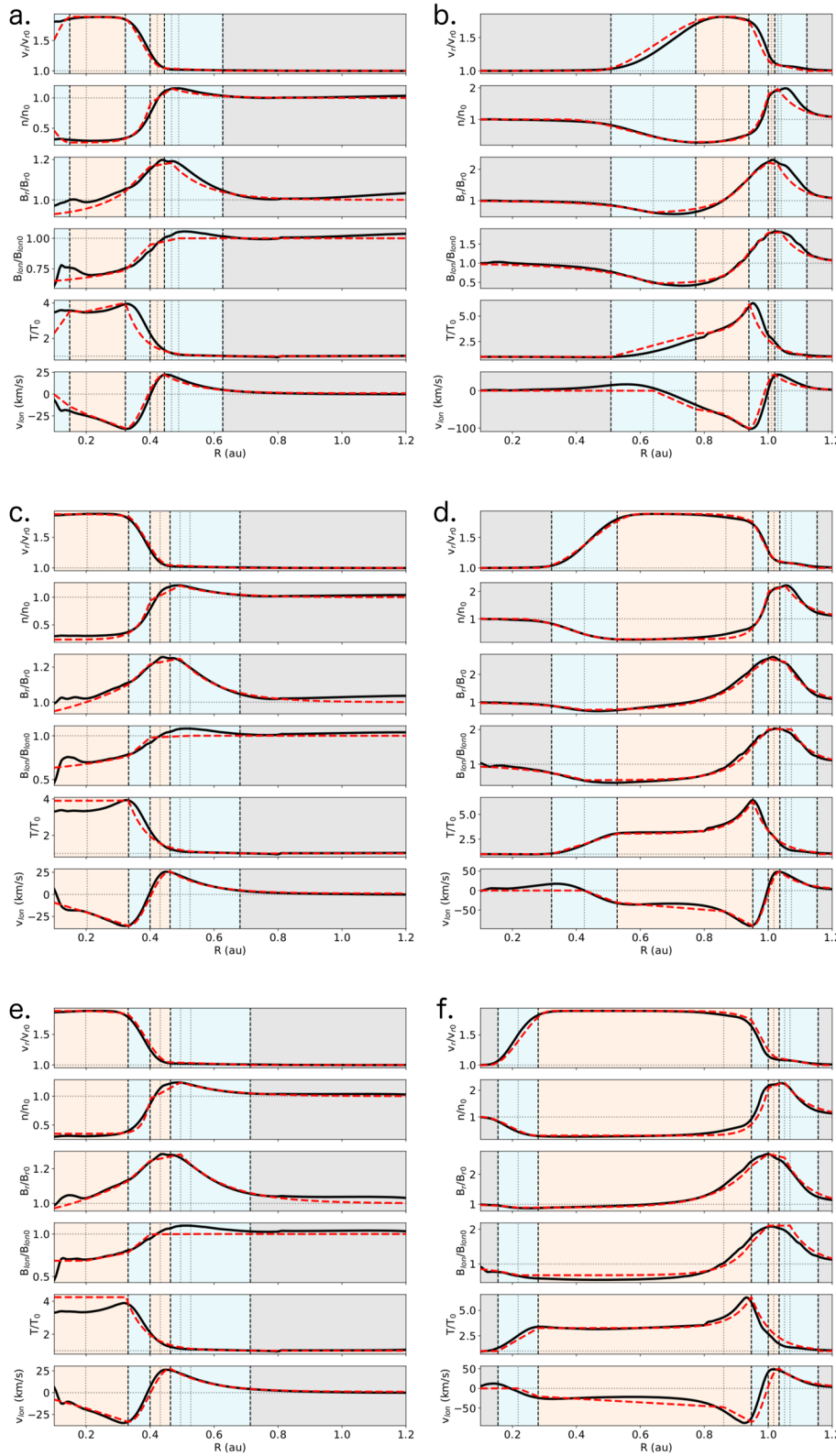

Figure 6. Comparsion of the magnetohydrodynamic and MEOW-HiSS results for different CH sizes and high speed stream front distances in the same format as Figure 3a. The rows show different areas with 3×10^{10} km^2 on top, 8×10^{10} km^2 in the middle, and 1.5×10^{11} km^2 at the bottom. The left column shows a front distance of 0.4 au and the right at 1.0 au.

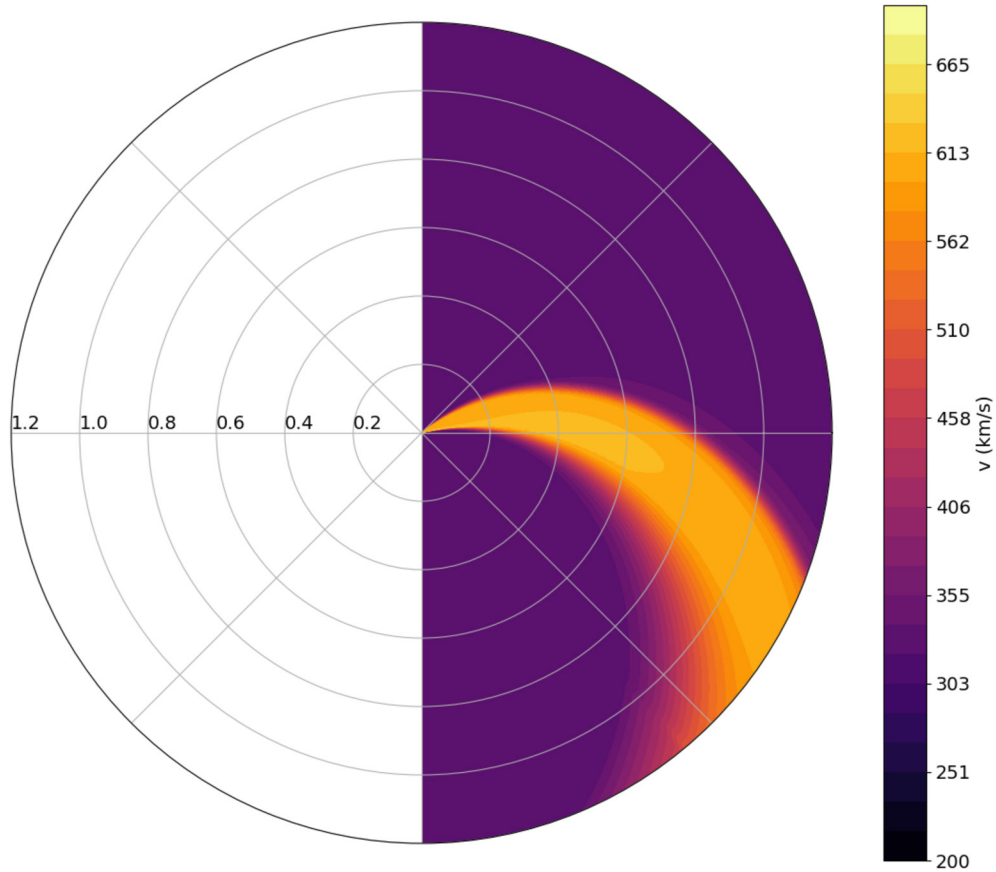

Figure 7. 2D visualization of MEOW-HiSS results showing contours of the radial velocity within the equatorial plane for an 8×10^{10} km^2 with the front at 1 au.

showing contours of the radial velocity. Similar visualizations can be produced for any of the MEOW-HiSS outputs. While these visualizations provide much of the same information as well-known simulations of the inner heliosphere such as ENLIL, we note that the MEOW-HiSS results can be obtained nearly instantaneously, which could be of use to gain context on the relative location of a HSS for space weather forecasting.

6. Application to 1 au HSS Forecasts

We hindcast several HSSs observed in situ at 1 au to demonstrate how MEOW-HiSS can be used for operational forecasts. We use the list of HSSs from Grandin et al. (2019) to select four recent events. These cases were selected as they had maximum speeds near 700 km/s, which was the maximum speed produced in most of the MHD simulations upon which MEOW-HiSS is based. Table 3 lists the start and end times of each event. In Grandin et al. (2019), the HSSs and their boundaries are automatically detected to form a large sample of nearly

Table 3
Properties of the Hindcast CMEs

In situ start	In situ end	Coronal start	CH area	Tuned SW params
19 September 2016 04:00	22 September 2016 22:00	16 September 2016 13:30	34	[8.0, 330, 2.5, 3.5, 50,000]
08 July 2017 23:00	12 July 2017 18:00	05 July 2017 19:32	52	[6.0, 330, 2.0, 2.0, 40,000]
03 August 2017 10:00	08 August 2017 04:00	31 July 2017 19:59	50	[4.5, 350, 2.0, 3.0, 40,000]
20 November 2017 12:00	24 November 2017 13:00	17 November 2017 13:49	26	[10.0, 330, 1.0, 1.5, 30,000]

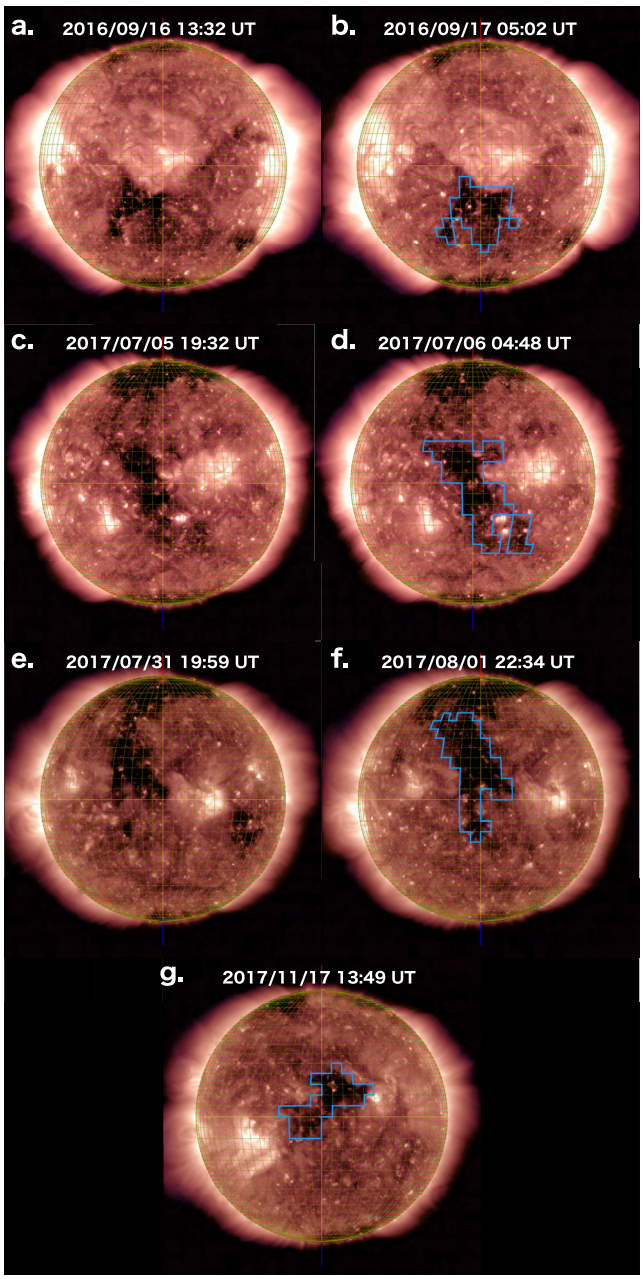

Figure 8. Solar dynamics observatory/atmospheric imaging assembly images combining the 193 and 211 Å channels that were used to generate the MEOW-HiSS input parameters. Each row shows a different case corresponding to the four different observed high speed streams. The left column shows the time of first contact between the CH and the Sun–Earth line. The right column shows the CH when it is centered around the central meridian, which should minimize any projection effects when estimating the CH area. The grid cells included in the CH area are outlined in light blue. For the November 2017 case, these two times are the same and we show a single image in panel (g).

600 events. We use the listed times to find each event within OMNI data, but revise the boundaries based on our own interpretation of the observations.

We have packaged MEOW-HiSS into a user-friendly tool that can provide a time series at 1 au using only the size of the corresponding CH and the time at which the solar rotation causes it to make first contact with the Sun–Earth line (which corresponds to a distance of 1 solar radii or approximately 0 au). While difficult to define with great precision, these two values can be fairly easily estimated from extreme ultra-violet (EUV) images of the solar disk. We acknowledge that defining these values may be significantly subject to user/forecaster interpretation, much like reconstructing CME positions from coronagraph images (e.g., Verbeke et al., 2022).

We make use of the JHelioviewer visualization software (Müller et al., 2017) to determine the MEOW-HiSS inputs. We note that while JHelioviewer has observations within a few days of the current date, one may need to develop an analogous routine using real time data to maximize the lead time for any actual forecast. With JHelioviewer we analyze EUV images from the Atmospheric Imaging Assembly (AIA; Lemen et al., 2012) on board the Solar Dynamics Observatory (SDO; Pesnell et al., 2012). The CHs appear with the most contrast in 193 Å, but have larger area in 211 Å. Through trial and error we have decided to display a background image of 193 Å overlayed with an image of 211 Å at 50% opacity. We turn on the grid feature within JHelioviewer and set it to show cells of $5° \times 5°$ resolution on the solar surface. We start searching for each source CH 4 days before the corresponding arrival at 1 au.

We first find the time at which a "significant" part of the CH reaches the central meridian, which should roughly correspond to a Sun–Earth connection. Figures 8a, 8c, 8e, and 8g show these visualizations from JHelioviewer at this time of first contact for each observed event. We note that this is an extremely subjective measurement, as we have tended to take the first time at which part of the CH touches the central meridian at the equator, if possible. In the case of the September 2016 event, the CH does not extend to the equator so we use the time at which the tip of a maximally extended region on the leading side of the CH reaches the central meridian.

The second step is to determine the CH area, which we can estimate using the grid cells. Each grid cell corresponds to an area of 3.7×10^9 km^2, hence we simply count the number of grid cells in the corresponding dark region. We perform this measurement at the time at which the CH surrounds the central meridian, the optimal viewing angle to minimize any projection effects from the Earth's perspective. Figures 8b, 8d, 8f, and 8g show this time while displaying the regions that we include in CH area outlined in light blue. We find that generously including any region with significant darkening tends to produce the most accurate in situ results. Note that we have a single image for the November 2017 case (Figure 8g) as the first contact and optimal viewing angle times occur simultaneously.

Table 3 lists the coronal start time and CH area (in grid cells) for each case, which we input into MEOW-HiSS. We still need to set up an empirical ambient background to scale the results to physical units. Since we are only considering results at 1 au we only need the ambient solar wind properties at that point, not a full profile. We consider two options—a default option based on average slow solar wind properties and tuning the background model based on the ambient wind upstream of the observed HSS. For the default option, we take the midpoints of the ranges given in Owens (2020): a number density of 7.5 cm^{-3}, radial velocity of 350 km/s, radial and longitudinal magnetic field of 4.2 nT, and temperature of 75×10^3 K. We assume

no longitudinal flow. The tuned values are determined by eye and included as an array with the same format units as listed above for the default values.

Figure 9 presents the results for the four cases. Within each subfigure the panels show the solar wind parameters in the same order as Figures 3–6, but the x-axes have changed to show time profiles instead of radial profiles. The black line shows the OMNI data, the red line shows the MEOW-HiSS results using the tuned ambient solar wind values, and the blue line shows the results using the default ambient solar wind values. Note that both the magnetic field and the longitudinal flow panels show the absolute values as MEOW-HiSS does not have the capability of predicting their directions. The background shading indicates which region is currently passing over the synthetic spacecraft, analogous to the regions identified within the radial profiles in Figures 3–6. We immediately see that, despite its simplicity, MEOW-HiSS can fairly accurately reproduce the observed data. The model consistently reproduces the timing and duration of the SIR, the plateau, and the tail. The general behavior is reproduced for each parameter. The density is very accurate within the plateau and tail for all cases, although we tend to underestimate the compression within the SIR. In half of the cases (Figures 9a and 9d) this is a small underestimate, but in the other half (Figures 9b and 9c) it is much more significant. The observed radial velocity profiles exhibit more variation than in MEOW-HiSS. For two of the cases (Figures 9b and 9d), the model tends to predict a sharper rise in v_r than seen in the data. Note there is no correlation between these two cases and the two with underestimated compression within the SIR. The tail is well-reproduced, with a slight tendency to underpredict its duration. The magnetic field is reproduced adequately, even though the observations do not have the strongest signatures in either B_r or B_{lon}. The most noticeable feature is an enhancement within the SIR, but the field also exhibits turbulent fluctuations during this time. There tends to be general agreement between MEOW-HiSS and the observations for both magnetic field observations, but the model does not include any turbulent fluctuations. MEOW-HiSS also reproduces the general behavior of the observed temperature for all cases. The timing of the peak in temperature is fairly accurate, but the magnitude is slightly underestimated in most cases. We continue to see a slight underestimate throughout the plateau. The observed profiles exhibit some structure and fluctuations beyond the scope of what MEOW-HiSS is capable of reproducing. In contrast to the other parameters, MEOW-HiSS does a rather poor job of simulating the longitudinal flow. We noted already that this was the worst parameter in terms of reproducing the MHD profiles, but that was primarily an issue of timing and not magnitude. For most cases, MEOW-HiSS significantly overestimates these flows. In many of the observations, there is little to no evidence of a reversal in the flow in the SIR in front of the HSS, yet the model predicts flows of 50–100 km/s, which are also seen in the MHD results. This remains an open issue, but we find that MEOW-HiSS is not a reliable option for accurately simulating observed longitudinal flows within a HSS.

In terms of the arrival time of the frontmost part of the SIR (x_1), we find errors of 4, 9, 4, and 4 hr for the four cases (in chronological order). Measuring an exact front is somewhat subjective, however, as the parameters slowly change as they approach peak values within the SIR or at the plateau. If we instead consider the position of the HSS front (x_3 or the reversal in v_{lon} in the OMNI data), we find errors of 1, 4, 2, and 1 hr. Note that both the OMNI and MEOW-HiSS values are in hourly resolution, hence the minimal precision in these errors.

We also quantify the errors in reproducing these observations, both using the tuned and default ambient solar wind parameters. Table 4 lists the MAFE in physical units for both the tuned and default ("tun" and "def") for all four cases ("September 16," "July 17," "August 17," and "November 17," chronologically). For each parameter we show the result in physical units, which are more useful for forecasting errors, and as a percentage, for comparison with the MAFE calculated with respect to the MHD profiles. We see that the tuned model tends to outperform the default model, but the difference is not particularly significant in most cases. We do see examples of the default option outperforming the tuned model, which occurs when an error in the input balances out an error in the model. The percentage errors show that we tend to find about 10% error in the radial velocity, of order 50% in the density, magnetic field, and temperature, and about 250% in the longitudinal flow. We find that our errors comparing MEOW-HiSS results and an observed HSS are roughly 5 times higher than comparing it with the MHD results. Averaging over all four default cases we find that MEOW-HiSS could currently provide in situ HSS forecasts with accuracies of 56.7 km/s in the radial velocity, 2.8 cm^{-3} in the number density, 2.2 nT in the absolute radial magnetic field, 1.6 nT in the absolute longitudinal magnetic field, and 7×10^4 K in the temperature. We cannot recommend using the longitudinal velocity for predictions. We also caution that these values are from four semi-arbitrary test cases with optimal maximum velocities and further study must be done with more cases and real-time EUV imagery to better validate MEOW-HiSS as a forecasting tool.

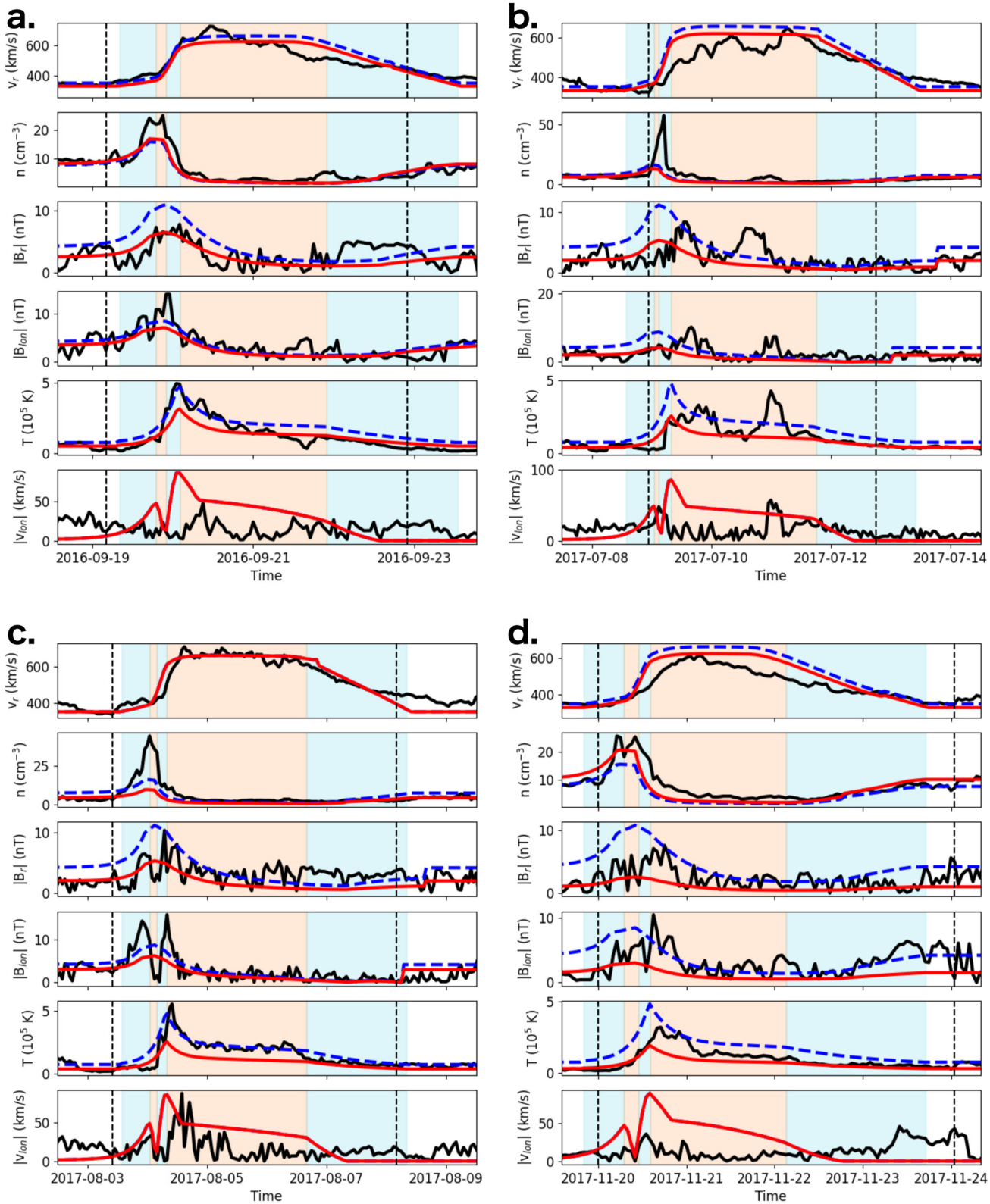

Figure 9. Comparison of the MEOW-HiSS results to the observed in situ profiles at 1 au for the four observed high speed stream (HSS). The panels have a format analogous to Figure 3 but show a profile in time rather than with respect to radial distance. Each panel includes the OMNI results (black), the MEOW-HiSS results using the tuned SW parameters (red), and the MEOW-HiSS results using the default SW parameters (blue dashed). The vertical dashed lines indicate the observed in situ HSS start and stop times.

Table 4
Hindcast Errors

Parameter	16 September tune	16 September def	17 July tune	17 July def	17 August tune	17 August def	November 17 tune	17 November def
v_r (km/s)	42.0	48.6	53.7	85.9	26.2	26.2	44.3	65.6
(%)	8.0	9.3	10.3	16.4	4.7	4.7	9.7	14.4
n (cm^{-3})	1.8	1.9	3.9	3.5	3.9	2.9	2.3	2.7
(%)	29.8	32.0	62.7	57.0	62.3	46.7	31.6	36.7
$\lvert B_r \rvert$ (nT)	1.6	2.4	1.9	2.1	2.0	2.1	1.5	2.2
(%)	52.3	77.3	64.6	72.0	61.3	64.5	66.2	93.6
$\lvert B_{lon} \rvert$ (nT)	1.4	1.3	2.0	2.1	1.6	1.5	2.2	1.6
(%)	39.8	35.3	70.6	72.1	56.5	50.9	66.4	47.8
T (10^5 K)	0.5	0.6	0.6	0.9	0.7	0.4	0.4	0.7
(%)	31.9	42.2	39.1	54.5	42.9	25.0	36.2	72.1
$\lvert v_{lon} \rvert$ (km/s)	40.2	40.2	48.2	48.2	40.0	40.0	37.1	37.1
(%)	280	280	286	286	254	254	264	264

7. Discussion

We have shown that MEOW-HiSS can accurately reproduce the MHD HSS profiles across a wide range of CH areas and front distances as well as hindcast HSSs that have been observed in situ at 1 au. We emphasize that MEOW-HiSS is simply a collection of empirical functions that will not shed any new light on the fundamental nature of the solar wind itself. On the other hand, the MHD model itself is not a perfectly accurate representation of the actual solar wind. At best, MEOW-HiSS can provide a profile matching the accuracy of the original MHD model to the real solar wind, and it will inherit all of the limitations of the MHD model. We find that MEOW-HiSS can reproduce the MHD results within about 10%, which corresponds to reproducing observed HSS with about 50% accuracy. MEOW-HiSS is a useful tool, however, that can be coupled with other models allowing for much more sophisticated, time-dependent solar wind backgrounds than previously possible through other backgrounds with similar computational requirements. This could lead to major improvements in our ability to forecast the space weather effects of CMEs, a suggestion we will explore in future works.

An additional aspect of MEOW-HiSS is its suitability for ensemble forecasts. Since it runs essentially instantaneously, it is no challenge to run a large number of simulations. We have provided a method for determining the necessary inputs for a 1 au forecast (area and timing) but these values are at best estimated, not precisely known. It is straightforward to run a series of MEOW-HiSS simulations with varying inputs to determine a range of uncertainties. This is important for forecasting the HSS itself, but also as a part of the background wind for any CME simulations. MEOW-HiSS has already been integrated within the OSPREI model (Kay, Mayes, & Collado-Vega, 2022) and we will present ensemble results of a CME–HSS interaction in a future work.

Another interesting aspect of MEOW-HiSS is that it could be run backwards in time. The only physics-driven component is the relation between distance, velocity, and time used for the boundaries, so all processes are entirely reversible. MEOW-HiSS can be used to back-map structures to the inner boundary at 0.1 au, which could then be combined with coronal models to identify solar sources. We note that propagating backward within a coronal model tends to be more difficult as the structure tends to vary more with different input parameters so that a small change can potentially lead to a drastically different back-mapping between 0.1 au and the solar surface.

8. Conclusion

We have introduced MEOW-HiSS, a new time-dependent model for a HSS. MEOW-HiSS is based on a set of MHD simulations with varying-size, idealized CHs. By breaking the MHD profiles into small regions we can reproduce nearly the full behavior of the MHD simulation using simple functions and a series of regressions that incorporate the effects of time and CH area. If given the CH area and the front of the HSS, MEOW-HiSS can produce radial profiles of the number density, radial and longitudinal velocity as well as magnetic field, and

temperature. This profile is not limited to the time corresponding to the provided front distance; MEOW-HiSS can also produce profiles at any subsequent time. In contrast to running a full MHD simulation, which could take up to tens of hours of computational time, MEOW-HiSS can calculate the HSS properties at a million different times and distances in under 3 min.

We have compared MEOW-HiSS results to the original MHD model. The quality ranges with different CH areas and HSS front distances. The lowest accuracy occurs when these values are near the extremes of the ranges that were used to develop the regressions. We typically see errors less than 10% for HSS distances below 1.5 au, but beyond this point the regressions become unstable and MEOW-HiSS should not be used. We find particularly good fits to the radial velocity. The simple functions have some difficulty reproducing the exact profiles of the longitudinal velocity across all front distances and CH areas, causing it to feature errors roughly an order of magnitude higher than the other parameters.

While accurately reproducing the MHD results is in itself useful, we show that MEOW-HiSS can be used to hindcast HSS observed in situ at 1 au. We present an algorithm that could be used in a real time scenario to determine the necessary inputs (CH area and start time of the HSS at the Sun). We then run MEOW-HiSS and determine the average accuracies over the full profile. We find average accuracies of 56.7 km/s in the radial velocity, 2.8 cm^{-3} in the number density, 2.2 nT in the absolute radial magnetic field, 1.6 nT in the absolute longitudinal magnetic field, and 7×10^4 K in the temperature.

Data Availability Statement

The MEOW-HiSS model is publicly available at github.com/ckay314/OSPREI as a part of the OSPREI package. The version of MEOW-HiSS used for this paper is archived through Zenodo at https://doi.org/10.5281/zenodo.7775180.

Acknowledgments
C. Kay is supported by the National Aeronautics and Space Administration under Grant 80NSSC19K0909 issued through the Heliophysics Early Career Investigators Program. C. Kay and E. Palmerio acknowledge support from NASA PSP-GI Grant 80NSSC22K0349. The work of T. Nieves-Chinchilla is supported by Heliophysics Innovation Funding (HIF) Program and the Solar Orbiter mission. E. Palmerio also acknowledges NASA LWS-SC Grant 80NSSC22K0893 and NSF PREEVENTS Grant ICER-1854790. We acknowledge use of NASA/GSFC's Space Physics Data Facility's OMNIWeb service, and OMNI data accessed at https://omniweb.gsfc.nasa.gov/ in early 2023. The JHelioviewer software was downloaded from www.jhelioviewer.org.

References

Arge, C. N., Luhmann, J. G., Odstrcil, D., Schrijver, C. J., & Li, Y. (2004). Stream structure and coronal sources of the solar wind during the May 12th, 1997 CME. *Journal of Atmospheric and Solar-Terrestrial Physics*, *66*(15–16), 1295–1309. https://doi.org/10.1016/j.jastp.2004.03.018

Augusto, C. R. A., Navia, C. E., de Oliveira, M. N., Nepomuceno, A. A., Raulin, J. P., Tueros, E., et al. (2018). The 2015 summer solstice storm: One of the major geomagnetic storms of solar cycle 24 observed at ground level. *Solar Physics*, *293*(5), 84. https://doi.org/10.1007/s11207-018-1303-8

Bale, S. D., Badman, S. T., Bonnell, J. W., Bowen, T. A., Burgess, D., Case, A. W., et al. (2019). Highly structured slow solar wind emerging from an equatorial coronal hole. *Nature*, *576*(7786), 237–242. https://doi.org/10.1038/s41586-019-1818-7

Belcher, J. W., & Davis, J. L. (1971). Large-amplitude Alfvén waves in the interplanetary medium, 2. *Journal of Geophysical Research*, *76*(16), 3534–3563. https://doi.org/10.1029/JA076i016p03534

Cranmer, S. R. (2009). Coronal holes. *Living Reviews in Solar Physics*, *6*(1), 3. https://doi.org/10.12942/lrsp-2009-3

Cranmer, S. R., Gibson, S. E., & Riley, P. (2017). Origins of the ambient solar wind: Implications for space weather. *Space Science Reviews*, *212*(3–4), 1345–1384. https://doi.org/10.1007/s11214-017-0416-y

Echer, E., Tsurutani, B. T., & Gonzalez, W. D. (2013). Interplanetary origins of moderate (−100 nT<Dst ≤−50 nT) geomagnetic storms during solar cycle 23 (1996-2008). *Journal of Geophysical Research: Space Physics*, *118*(1), 385–392. https://doi.org/10.1029/2012JA018086

Einaudi, G., Boncinelli, P., Dahlburg, R. B., & Karpen, J. T. (1999). Formation of the slow solar wind in a coronal streamer. *Journal of Geophysical Research*, *104*(A1), 521–534. https://doi.org/10.1029/98JA02394

Fisk, L. A. (2003). Acceleration of the solar wind as a result of the reconnection of open magnetic flux with coronal loops. *Journal of Geophysical Research*, *108*(A4), 1157. https://doi.org/10.1029/2002JA009284

Gerontidou, M., Mavromichalaki, H., & Daglis, T. (2018). High-speed solar wind streams and geomagnetic storms during solar cycle 24. *Solar Physics*, *293*(9), 131. https://doi.org/10.1007/s11207-018-1348-8

Gonzalez, W. D., Tsurutani, B. T., & Clúa de Gonzalez, A. L. (1999). Interplanetary origin of geomagnetic storms. *Space Science Reviews*, *88*(3/4), 529–562. https://doi.org/10.1023/A:1005160129098

Grandin, M., Aikio, A. T., & Kozlovsky, A. (2019). Properties and geoeffectiveness of solar wind high-speed streams and stream interaction regions during solar cycles 23 and 24. *Journal of Geophysical Research: Space Physics*, *124*(6), 3871–3892. https://doi.org/10.1029/2018JA026396

Gressl, C., Veronig, A. M., Temmer, M., Odstrčil, D., Linker, J. A., Mikić, Z., & Riley, P. (2014). Comparative study of MHD modeling of the background solar wind. *Solar Physics*, *289*(5), 1783–1801. https://doi.org/10.1007/s11207-013-0421-6

Harra, L. K., Sakao, T., Mandrini, C. H., Hara, H., Imada, S., Young, P. R., et al. (2008). Outflows at the edges of active regions: Contribution to solar wind formation? *The Astrophysical Journal Letters*, *676*(2), L147–L150. https://doi.org/10.1086/587485

Heinemann, S. G., Temmer, M., Farrugia, C. J., Dissauer, K., Kay, C., Wiegelmann, T., et al. (2019). CME-HSS interaction and characteristics tracked from Sun to Earth. *Solar Physics*, *294*(9), 121. https://doi.org/10.1007/s11207-019-1515-6

Hofmeister, S. J., Asvestari, E., Guo, J., Heidrich-Meisner, V., Heinemann, S. G., Magdalenic, J., et al. (2022). How the area of solar coronal holes affects the properties of high-speed solar wind streams near Earth: An analytical model. *Astronomy & Astrophysics*, *659*, A190. https://doi.org/10.1051/0004-6361/202141919

Hofmeister, S. J., Veronig, A. M., Poedts, S., Samara, E., & Magdalenic, J. (2020). On the dependency between the peak velocity of high-speed solar wind streams near Earth and the area of their solar source coronal holes. *The Astrophysical Journal Letters*, *897*(1), L17. https://doi.org/10.3847/2041-8213/ab9d19

Jian, L. K., MacNeice, P. J., Taktakishvili, A., Odstrcil, D., Jackson, B., Yu, H. S., et al. (2015). Validation for solar wind prediction at Earth: Comparison of coronal and heliospheric models installed at the CCMC. *Space Weather*, *13*(5), 316–338. https://doi.org/10.1002/2015SW001174
Jian, L. K., Russell, C. T., & Luhmann, J. G. (2011). Comparing solar minimum 23/24 with historical solar wind records at 1 AU. *Solar Physics*, *274*(1–2), 321–344. https://doi.org/10.1007/s11207-011-9737-2
Jin, M., Manchester, W. B., van der Holst, B., Sokolov, I., Tóth, G., Mullinix, R. E., et al. (2017). Data-constrained coronal mass ejections in a global magnetohydrodynamics model. *The Astrophysical Journal*, *834*(2), 173. https://doi.org/10.3847/1538-4357/834/2/173
Kataoka, R., Shiota, D., Kilpua, E., & Keika, K. (2015). Pileup accident hypothesis of magnetic storm on 17 March 2015. *Geophysical Research Letters*, *42*(13), 5155–5161. https://doi.org/10.1002/2015GL064816
Kay, C., Mays, M. L., & Collado-Vega, Y. M. (2022). OSPREI: A coupled approach to modeling CME-driven space weather with automatically generated, user-friendly outputs. *Space Weather*, *20*(4), e2021SW002914. https://doi.org/10.1029/2021SW002914
Kay, C., & Nieves-Chinchilla, T. (2021). Modeling interplanetary expansion and deformation of CMEs with ANTEATR PARADE: Relative contribution of different forces. *Journal of Geophysical Research: Space Physics*, *126*(5), e2020JA028911. https://doi.org/10.1029/2020JA028911
Kay, C., Nieves-Chinchilla, T., Hofmeister, S. J., & Palmerio, E. (2022). Beyond basic drag in interplanetary CME modeling: Effects of solar wind pileup and high-speed streams. *Space Weather*, *20*(9), e2022SW003165. https://doi.org/10.1029/2022SW003165
Lemen, J. R., Title, A. M., Akin, D. J., Boerner, P. F., Chou, C., Drake, J. F., et al. (2012). The atmospheric imaging assembly (AIA) on the solar dynamics observatory (SDO). *Solar Physics*, *275*(1–2), 17–40. https://doi.org/10.1007/s11207-011-9776-8
Maharana, A., Isavnin, A., Scolini, C., Wijsen, N., Rodriguez, L., Mierla, M., et al. (2022). Implementation and validation of the FRi3D flux rope model in EUHFORIA. *Advances in Space Research*, *70*(6), 1641–1662. https://doi.org/10.1016/j.asr.2022.05.056
Mays, M. L., Taktakishvili, A., Pulkkinen, A., MacNeice, P. J., Rastätter, L., Odstrcil, D., et al. (2015). Ensemble modeling of CMEs using the WSA-ENLIL+Cone model. *Solar Physics*, *290*(6), 1775–1814. https://doi.org/10.1007/s11207-015-0692-1
Mikić, Z., Linker, J. A., Schnack, D. D., Lionello, R., & Tarditi, A. (1999). Magnetohydrodynamic modeling of the global solar corona. *Physics of Plasmas*, *6*(5), 2217–2224. https://doi.org/10.1063/1.873474
Müller, D., Nicula, B., Felix, S., Verstringe, F., Bourgoignie, B., Csillaghy, A., et al. (2017). JHelioviewer. Time-dependent 3D visualisation of solar and heliospheric data. *Astronomy & Astrophysics*, *606*, A10. https://doi.org/10.1051/0004-6361/201730893
Odstrcil, D. (2003). Modeling 3-D solar wind structure. *Advances in Space Research*, *32*(4), 497–506. https://doi.org/10.1016/S0273-1177(03)00332-6
Owens, M. J. (2020). *Solar-wind structure*. Oxford University Press. https://doi.org/10.1093/acrefore/9780190871994.013.19
Owens, M. J., Lang, M., Barnard, L., Riley, P., Ben-Nun, M., Scott, C. J., et al. (2020). A computationally efficient, time-dependent model of the solar wind for use as a surrogate to three-dimensional numerical magnetohydrodynamic simulations. *Solar Physics*, *295*(3), 43. https://doi.org/10.1007/s11207-020-01605-3
Palmerio, E., Lee, C. O., Richardson, I. G., Nieves-Chinchilla, T., Dos Santos, L. F. G., Gruesbeck, J. R., et al. (2022). CME evolution in the structured heliosphere and effects at Earth and Mars during solar minimum. *Space Weather*, *20*(9), e2022SW003215. https://doi.org/10.1029/2022SW003215
Pesnell, W. D., Thompson, B. J., & Chamberlin, P. C. (2012). The solar dynamics observatory (SDO). *Solar Physics*, *275*(1–2), 3–15. https://doi.org/10.1007/s11207-011-9841-3
Pinto, R. F., & Rouillard, A. P. (2017). A multiple flux-tube solar wind model. *The Astrophysical Journal*, *838*(2), 89. https://doi.org/10.3847/1538-4357/aa6398
Pizzo, V., Millward, G., Parsons, A., Biesecker, D., Hill, S., & Odstrcil, D. (2011). Wang-Sheeley-Arge-Enlil Cone model transitions to operations. *Space Weather*, *9*(3), 03004. https://doi.org/10.1029/2011SW000663
Pomoell, J., & Poedts, S. (2018). EUHFORIA: European heliospheric forecasting information asset. *Journal of Space Weather and Space Climate*, *8*, A35. https://doi.org/10.1051/swsc/2018020
Pulkkinen, T. (2007). Space weather: Terrestrial perspective. *Living Reviews in Solar Physics*, *4*(1), 1. https://doi.org/10.12942/lrsp-2007-1
Reiss, M. A., Muglach, K., Mullinix, R., Kuznetsova, M. M., Wiegand, C., Temmer, M., et al. (2022). Unifying the validation of ambient solar wind models. *Advances in Space Research*, in press. https://doi.org/10.1016/j.asr.2022.05.026
Richardson, I. G. (2018). Solar wind stream interaction regions throughout the heliosphere. *Living Reviews in Solar Physics*, *15*(1), 1. https://doi.org/10.1007/s41116-017-0011-z
Richardson, I. G., Webb, D. F., Zhang, J., Berdichevsky, D. B., Biesecker, D. A., Kasper, J. C., et al. (2006). Major geomagnetic storms (Dst ≤ -100 nT) generated by corotating interaction regions. *Journal of Geophysical Research*, *111*(A7), A07S09. https://doi.org/10.1029/2005JA011476
Richardson, I. G., Wibberenz, G., & Cane, H. V. (1996). The relationship between recurring cosmic ray depressions and corotating solar wind streams at ≤ 1 AU: IMP 8 and Helios 1 and 2 anticoincidence guard rate observations. *Journal of Geophysical Research*, *101*(A6), 13483–13496. https://doi.org/10.1029/96JA00547
Riley, P., & Ben-Nun, M. (2022). sunRunner1D: A tool for exploring ICME evolution through the inner heliosphere. *Universe*, *8*(9), 447. https://doi.org/10.3390/universe8090447
Riley, P., Linker, J. A., Lionello, R., & Mikic, Z. (2012). Corotating interaction regions during the recent solar minimum: The power and limitations of global MHD modeling. *Journal of Atmospheric and Solar-Terrestrial Physics*, *83*, 1–10. https://doi.org/10.1016/j.jastp.2011.12.013
Riley, P., & Luhmann, J. G. (2012). Interplanetary signatures of unipolar streamers and the origin of the slow solar wind. *Solar Physics*, *277*(2), 355–373. https://doi.org/10.1007/s11207-011-9909-0
Schwadron, N. A., McComas, D. J., Elliott, H. A., Gloeckler, G., Geiss, J., & von Steiger, R. (2005). Solar wind from the coronal hole boundaries. *Journal of Geophysical Research*, *110*(A4), A04104. https://doi.org/10.1029/2004JA010896
Temmer, M. (2021). Space weather: The solar perspective. *Living Reviews in Solar Physics*, *18*(1), 4. https://doi.org/10.1007/s41116-021-00030-3
Török, T., Downs, C., Linker, J. A., Lionello, R., Titov, V. S., Mikić, Z., et al. (2018). Sun-to-Earth MHD simulation of the 2000 July 14 "Bastille Day" eruption. *The Astrophysical Journal*, *856*(1), 75. https://doi.org/10.3847/1538-4357/aab36d
Tsurutani, B. T., Gonzalez, W. D., Gonzalez, A. L. C., Guarnieri, F. L., Gopalswamy, N., Grande, M., et al. (2006). Corotating solar wind streams and recurrent geomagnetic activity: A review. *Journal of Geophysical Research*, *111*(A7), A07S01. https://doi.org/10.1029/2005JA011273
van der Holst, B., Manchester, W. B., IV, Frazin, R. A., Vásquez, A. M., Tóth, G., & Gombosi, T. I. (2010). A data-driven, two-temperature solar wind model with Alfvén Waves. *The Astrophysical Journal*, *725*(1), 1373–1383. https://doi.org/10.1088/0004-637X/725/1/1373
van der Holst, B., Sokolov, I. V., Meng, X., Jin, M., Manchester, W. B., IV., Tóth, G., & Gombosi, T. I. (2014). Alfvén wave solar model (AWSoM): Coronal heating. *The Astrophysical Journal*, *782*(2), 81. https://doi.org/10.1088/0004-637X/782/2/81
Verbeke, C., Mays, M. L., Kay, C., Riley, P., Palmerio, E., Dumbović, M., et al. (2022). Quantifying errors in 3D CME parameters derived from synthetic data using white-light reconstruction techniques. *Advances in Space Research*. in press. https://doi.org/10.1016/j.asr.2022.08.056
Verbeke, C., Mays, M. L., Temmer, M., Bingham, S., Steenburgh, R., Dumbović, M., et al. (2019). Benchmarking CME arrival time and impact: Progress on metadata, metrics, and events. *Space Weather*, *17*(1), 6–26. https://doi.org/10.1029/2018SW002046

Vršnak, B., Žic, T., Vrbanec, D., Temmer, M., Rollett, T., Möstl, C., et al. (2013). Propagation of interplanetary coronal mass ejections: The drag-based model. *Solar Physics*, *285*(1–2), 295–315. https://doi.org/10.1007/s11207-012-0035-4

Webb, D. F., & Howard, T. A. (2012). Coronal mass ejections: Observations. *Living Reviews in Solar Physics*, *9*, 3. https://doi.org/10.12942/lrsp-2012-3

Zhang, J., Richardson, I. G., Webb, D. F., Gopalswamy, N., Huttunen, E., Kasper, J. C., et al. (2007). Solar and interplanetary sources of major geomagnetic storms (Dst≤−100 nT) during 1996-2005. *Journal of Geophysical Research*, *112*(A10), A10102. https://doi.org/10.1029/2007JA012321